Interactions between irradiation defects and nitrogen in α-Fe: an integrated experimental and theoretical study

Published in Acta Materialia, doi:10.1016/j.actamat.2022.118227

Andreas Theodorou[a,b,*], Maria-Andromachi Syskaki[b], Zoi Kotsina[c], Michail Axiotis[c], George Apostolopoulos[b], Chu-Chun Fu[d]

[a] *Section of Solid State Physics, Department of Physics, National and Kapodistrian University of Athens, Panepistimiopolis, GR-157 84, Zografos, Greece*
[b] *Institute of Nuclear & Radiological Sciences & Technology, Energy & Safety, National Centre for Scientific Research "Demokritos", GR-153 10 Aghia Paraskevi, Greece*
[c] *Tandem Accelerator Laboratory, Institute of Nuclear and Particle Physics, National Centre for Scientific Research "Demokritos", GR-153 10, Agia Paraskevi, Greece*
[d] *Université Paris-Saclay, CEA, Service de Recherches de Métallurgie Physique, 91191 Gif-sur-Yvette, France*

Abstract

This paper aims at clarifying, by means of an integrated experimental and theoretical approach, the properties of the interaction between interstitial nitrogen (N) and irradiation generated lattice defects in α-Fe. For this purpose, N-doped and pure Fe specimens were irradiated at low temperature by high energy protons. The evolution of radiation defects and their interaction with N was monitored by electrical resistivity measurements during post-irradiation annealing. In parallel, density functional theory (DFT) was employed to study the properties of N solutes, vacancies and their mutual interaction in the Fe matrix. The DFT results were confronted to the experiment via kinetic rate theory modelling, employed to quantitatively simulate the measured resistivity evolution. One of the most important results is the experimental validation of the theoretically predicted strong binding energy of vacancy-N complexes, which reconciles previous discrepancies. Furthermore, a quantitative interpretation is provided of how irradiation competes with nitride precipitation.

Keywords: Iron, Nitrogen interstitial, Nitride precipitation, Defect - Nitrogen interaction, Proton Irradiation, Electrical Resistivity, Density functional theory, Reaction rate theory

1. Introduction

Nitrogen (N) along with carbon (C) are the most common foreign interstitial atoms (FIAs) in iron (Fe) and have a strong impact on the microstructure, mechanical properties and performance of steel [1]. When their concentration exceeds the solubility limits, they tend to precipitate into nitrides and carbides, respectively, altering the macroscopic properties such as the strength and hardness. Under irradiation, the interaction of intrinsic lattice defects with FIAs has a significant impact on the damage and recovery processes in Fe and ferritic steels. Defects can form stable clusters with FIAs and thus interfere with precipitation reactions and phase stability. These effects have been studied experimentally by a number of workers [2–12]. More recently there have been also significant efforts to understand the defect-FIA interactions theoretically [13–19], within the general aim to predict the life time of irradiated materials in nuclear energy systems by means of modelling and simulation [20, 21]. However, despite considerable effort, the mechanism of these interactions, especially for N, is not yet fully understood.

The trapping of mobile N solute atoms by radiation defects at temperatures between 295 and 315 K has been observed by magnetic disaccommodation [5], internal friction [7] and magnetic after effect (MAE) [11] measurements in electron and neutron irradiated, dilute Fe-N alloys. Most authors assumed that the trapping was due to lattice vacancies (V) [7, 11], which they regarded as immobile at these temperatures; however, self interstitial atom (SIA) clusters were also considered as trapping centers [5]. The release of N back into the matrix was observed at temperatures between 420 and 500 K with an activation energy, Q_d, between 0.85 and 1.4 eV [7, 11]. Since N was believed to be the most mobile constituent of the N-V clusters, the N migration barrier, in the range 0.76-0.8 eV, was subtracted from Q_d and, hence, the N-V binding energy was obtained in the range 0.1 to 0.5 eV [11]. More recent electrical resistivity experiments in electron irradiated, N-doped Fe [12] also indicated values of 0.1-0.15 eV. On the other hand, the stability of vacancy-N complexes in Fe has been investigated in detail also by *ab initio* theoretical methods. These calculations showed systematically higher values for the VN binding energy, 0.71 [13] and 0.73 eV [17], making it difficult to reconcile theory with experiment.

In Fe-N alloys of higher concentration, where nitride precipitation takes place, only a few irradiation experiments have been reported. These mostly involved the metastable α''-$Fe_{16}N_2$ nitride, which forms either during low-temperature ($300 \lesssim T \leq 420$ K) ageing of supersaturated ferritic Fe-N or by tempering of nitrogen martensite [22, 23]. The α'' phase is particularly

*Corresponding author
Email address: theoda@ipta.demokritos.gr (Andreas Theodorou)

interesting due to its age hardening effects [24], stress orientation of precipitates [25, 26] and magnetic properties [23, 27]. The effect of electron irradiation on α'' precipitation has been studied by high voltage electron microscopy (HVEM) [6, 8]. In these experiments, it was observed that α'' precipitates did not form in the irradiated area of supersaturated Fe-N specimens after annealing at 400 to 430 K, whereas the un-irradiated regions of the same specimens showed ample precipitation. This was ascribed to the trapping of N atoms by vacancies generated by the irradiation. After annealing at 490 K for 15 minutes and re-ageing at 400 K, small precipitates appeared also in the irradiated area, indicating that dissociation of *V*N clusters occurred at 490 K. More detailed studies of irradiation effects on FIA precipitation were performed by Damask *et al.* on neutron irradiated Fe-C utilizing internal friction [2], electrical resistivity [3] and electron microscopy [4]. These experiments showed that, depending on the conditions, neutron irradiation may either provide nucleation sites and thereby promote carbide precipitation or produce defects that contribute to FIA trapping. However, due to the limited knowledge at that time of defect properties and interactions in Fe, a more accurate interpretation of these studies could not be given.

In this paper we address some of the issues mentioned above regarding the interaction of radiation defects with N in Fe, including precipitation effects, using electrical resistivity measurements. This method is highly sensitive to both radiation defects and precipitates and has been utilized extensively for the study of kinetics in metallic materials. In the case of Fe, resistivity recovery experiments after low temperature electron irradiation, as for example by Takaki *et al.* [10], were essential in clarifying point defect reactions in this material. A number of recovery stages, i.e., temperature ranges of increased defect annealing, were attributed to specific reaction mechanisms: stages I_D ($\sim$ 108 K) and I_E (120 - 140 K) were ascribed to the correlated and un-correlated, long-range migration of SIAs; stage II (160-180 K) to the migration of small SIA clusters; and stage III (220-280 K) was related to long-range vacancy migration. However, the quantitative interpretation of these experiments presents difficulties; as shown previoulsy in several works [15, 28], it requires detailed theoretical analysis in order to obtain reliable information on the underlying physical processes. Therefore, in the current work we adopt an integrated approach, combining experiment with theoretical modelling and simulation, in order to directly obtain clear and definite results. Specifically, specimens of an Fe - 0.048 at.% N alloy and a control sample of pure Fe were irradiated by 5 MeV protons at cryogenic temperature. High energy protons are being increasingly utilized for such studies [29–32] due to their relatively high penetration depth, which allows volume irradiation of specimens, and their high availability at ion accelerator facilities. The evolution of radiation induced defects and the precipitation of the metastable α''-$Fe_{16}N_2$ nitride were monitored by *in-situ* measurements of the electrical resistivity during post-irradiation isochronal annealing up to 550 K. Comparison between Fe-N and pure Fe gives information on the effect of N on defect kinetics.

For the interpretation of results, density function theory (DFT) calculations are used to characterize the binding between vacancy and N solute atoms as well as their kinetic properties. The evolution of defect and solute atom concentrations is described by reaction rate equations, while α'' precipitation is modelled by classical theory of nucleation and growth. Finally, a calculation of the total resistivity due to defects and precipitates allows direct comparison to the experiment.

The paper is organized as follows: Section 2 describes the sample preparation, the irradiation conditions and the post-irradiation annealing; the modelling methodology is given in section 3, including the DFT calculations, the kinetic equations for the evolution of precipitates and defects and the evaluation of the electrical resistivity; section 4 presents the experimental results while section 5 the simulation results; finally, a discussion is presented in section 6.

2. Samples and Experimental methods

2.1. Sample preparation

The materials investigated in this study were high purity Fe and Fe-N produced by the Ecole des Mines de Saint Etienne. Table 1 shows the concentration of interstitial elements in the materials as obtained from a chemical analysis conducted by the supplier. The concentrations of other residual impurities were generally below 5 appm. The Fe-N alloy is doped with N to a concentration of 480 appm, while the residual content of other interstitial impurities like carbon and oxygen is about 40 appm. In pure Fe there is a small amount of C (20 appm) and smaller amounts of N and O. Both materials were supplied in the form of 10.5 mm diameter cylindrical bars. Thin foils were produced by sectioning, cold-rolling and electropolishing in a H_2SO_4-H_3PO_4 mixture to a final thickness of 0.050 mm. The foils exhibit a bright polished surface after the electrochemical process. Rectangular specimens 15 mm $\times$ 2 mm were cut from the foils, placed in alumina crucibles and heat treated under oil-free high vacuum (10^{-6} mbar) at 970 K for 12 h in order to anneal stresses due to cold working. Fe-N specimens were subjected to a further special annealing procedure by means of ohmic self-heating. Specifically, a specimen was held inside a closed liquid nitrogen (LN) dewar, a few centimetres above the surface of the cryogenic liquid. A large electrical current was sent through the sample, heating it to a high temperature. Digital control of heating current and sample voltage allowed stabilization of the sample temperature to within ±2%. Fast quenching was possible by directly dipping the sample into LN. The actual annealing temperature was estimated from the sample resistivity, by comparing to tabulated values of the resistivity of Fe as a function of temperature [33]. Fe-N specimens were heated in this manner for 10 min at 863 K and then quenched, to ensure full dissolution of N in the Fe matrix. The specimens were kept in LN until further use. During loading in the irradiation chamber, they were heated to room temperature for about 2 h.

2.2. Electrical resistivity measurements

Pure Fe current and potential leads were spot-welded on the specimens for performing the electrical resistivity measure-

Table 1: Concentrations of interstitial elements (appm) in the starting materials.

Material	C	N	O
Fe	20	4	14
Fe-N	40	480	36

ments according to the standard DC four-probe method. The ohmic voltage was measured with a sensitive nano-voltmeter (Keithley Inc) and the measuring current was reversed in order to eliminate thermoelectric voltages. The measurement resolution was better than 10^{-7} Ω. Resistance, R, was converted to absolute resistivity, ρ, by means of the geometric factor, $f = \rho/R$. f was obtained for each specimen by taking two resistance measurements: one at 273 K using a temperature calibrator and one in LN at 77 K. These values are denoted as R_{273} and R_{77}, respectively. The geometric factor was then calculated by $f = (\rho^{Fe}_{273} - \rho^{Fe}_{77})/(R_{273} - R_{77})$, where $\rho^{Fe}_{273} = 8570$ nΩ·cm and $\rho^{Fe}_{77} = 612$ nΩ·cm correspond to tabulated values of pure Fe resistivity at the respective temperatures [33]. This method minimizes errors in f due to the residual resistivity of impure or dilute alloy samples. The estimated error in f is below 1%.

The reported resistivity measurements were generally taken at the base temperature of the irradiation chamber, 8 K, where phonon contribution is negligible. Thus, they correspond to the residual resistivity, which is mainly due to conduction electron scattering at lattice defects and solute atoms. Only during annealing of un-irradiated specimens the measurements were performed at liquid nitrogen temperature. However, since we are mainly interested in resistivity changes during the course of the annealing, the constant phonon contribution at 77 K cancels out.

The residual resistivity of the samples prior to the irradiation, ρ_0, and the residual resistivity ratio, RRR = $\rho(300\text{ K})/\rho_0$, are listed in Table 2. It is observed that there is a difference of 315±10 nΩ-cm in ρ_0 between Fe-N and Fe specimens. This is mainly due to the N solute atoms, which contribute 0.6 nΩ-cm per appm [34] or 290 nΩ-cm in total, taking into account the nominal N concentration. The increased concentrations of C and O in Fe-N (cf. Table 1) account for the rest of the observed resistivity difference. The residual resistivity of pure Fe is due to the small concentrations of interstitial and other residual impurities. Contributions to the electrical resistivity due to surface scattering can be ignored since the estimated electron mean free path in Fe at 8 K is much smaller than the sample thickness.

2.3. Irradiation conditions

Irradiations were performed in the dedicated materials irradiation facility IR^2 at the TANDEM accelerator of the National Centre for Scientific Research "Demokritos" [35]. The facility offers *in-situ* electrical resistivity measurement, irradiation at cryogenic temperature down to 8 K by means of a closed-cycle helium cryo-cooler and post-irradiation annealing up to 700 K. The specimens were irradiated with 5 MeV protons to three different dose levels. Details are given in Table 2. The actual specimen temperature during irradiation was estimated to be about 25±3 K due to beam heating. The estimation is based on online electrical resistivity measurements which showed a sudden increase of resistivity as the beam was switched on. This was converted to temperature based on the measured resistivity vs. temperature curve.

The irradiation time was adjusted so that the desired radiation induced resistivity increase, $\Delta\rho_0$, was attained. $\Delta\rho_0$ is proportional to the number of generated radiation defects and thus constitutes a direct measure of the damage dose for a given specimen. Hence, it was considered as a more reliable dose indicator than beam flux measurements, which were performed only intermittently using a Faraday cup and depend on a number of parameters that may vary between irradiations as, e.g., beam fluctuation or sample positioning. The amount of radiation damage in terms of displacements per atom (dpa) is estimated by dividing $\Delta\rho_0$ with the recommended value for the Frenkel pair resistivity in Fe, $\rho_{FP} = 3.0$ nΩ-cm / appm [36, 37]. As can be seen from the data of Table 2, the estimated concentration of radiation defects ranged from 33 to 330 appm. We note, however, that there is still some uncertainty regarding the value of ρ_{FP}, since other authors [38] and reference works [39] quote also different values. Thus the estimated dpa should be treated with caution. Further detailed measurements of ρ_{FP} are needed in order to clarify this discrepancy, which should be corroborated by theoretical calculations.

The irradiation conditions were simulated with the SRIM code [40] following the procedure described in [41, 42] and employing a displacement threshold of 40 eV [43]. The simulation shows that the 5 MeV proton range in Fe is about 0.08 mm, thus the beam penetrates fully through the 0.05 mm thick foils with negligible implantation probability. The damage profile as obtained by SRIM is fairly homogeneous within the sample volume, with the damage rate becoming gradually higher towards the back side of the specimen due to proton energy loss. The average recoil energy of primary knock-on atoms is 330 eV and, thus, the damage is expected to be primarily in the form of single vacancies and SIAs [44]. The damage cross-section as predicted by SRIM is 1.5×10^{-20} cm^2, while experimentally we obtain values between 0.6 and 0.9×10^{-20} cm^2. The latter can be obtained from Table 2 by taking the ratio of dpa to fluence. We consider that this is a fair agreement given the experimental uncertainty in the flux measurement and the known tendency of the Norgett-Robertson-Torrens (NRT) damage model [45] employed in SRIM to overestimate the dpa values [46].

2.4. Annealing procedure

Post-irradiation isochronal annealing was performed inside the irradiation chamber without removing the sample. Stepwise annealing was employed at gradually increasing temperatures from 40 up to 600 K, with a variable temperature step, ΔT, keeping $\Delta T/T \approx 0.04$. Holding time was 5 min for Fe, while Fe-N samples were given two 4 min anneals per temperature step. The latter procedure allowed the estimation of activation energies, as explained below. The annealing of irradiated Fe-N samples was also performed by the ohmic self-heating method as described in section 2.1. However, the quenching was achieved by simply switching off the heating current and allowing the sample to reach the base temperature (8 K) of the

Table 2: Conditions for the 5 MeV proton irradiation of Fe-N and Fe.

Material	ρ_0 [*] (nΩ-cm)	RRR [†]	Proton Flux (10^{11} cm^{-2} s^{-1})	Fluence (10^{15} cm^{-2})	$\Delta\rho_0$ [‡] ($n\Omega$-cm)	dpa / X^0_{FP} [§] (appm)
	420	25	3.7	3.7	100	33
Fe-N	410	25	4.2	20	500	165
	405	25	4.4	43	1000	330
Fe	95	110	9.0	5.4	100	33

[*] ρ_0: residual resistivity
[†] RRR = $\rho(300\ \mathrm{K})/\rho_0$
[‡] $\Delta\rho_0$: max. irradiation induced resistivity
[§] dpa: displacements per atom, X^0_{FP}: Frenkel pair (FP) concentration. Calculated as $\Delta\rho_0/\rho_{FP}$, where ρ_{FP} = 3.0 nΩ-cm / appm is the FP resistivity in Fe.

surrounding sample holder, whereupon the resistivity was re-measured. This method allowed fast heating and cooling at a rate up to ∼ 20 K/s and good temperature stabilization with an overshoot of less than 2%.

Un-irradiated specimens were subjected to isochronal annealing cycles from 250 up to 550 K with $\Delta T/T \approx 0.03$ and a holding time of 5 min. These were performed by self-heating and quenching in liquid nitrogen as described in section 2.1.

During the course of an annealing sequence, the resistivity of the sample, ρ, changes due to defect annihilation, clustering and solute precipitation. In the following we report the resistivity evolution, $\Delta\rho = \rho - \rho_0$, from its initial value, ρ_0, measured prior to the irradiation. For irradiated specimens wih an initial resistivity increase $\Delta\rho_0$, the ratio $\Delta\rho/\Delta\rho_0$ is termed resistivity recovery and is roughly proportional to the fraction of radiation defects remaining in the specimen at a certain stage of the annealing program. In case of clustering and precipitation reactions the relation of $\Delta\rho$ to defect and solute atom concentrations may be more complex.

The activation energy, E_a, of annealing reactions in Fe-N was estimated by the slope-change technique [47, 48]. For this purpose, Fe-N specimens were given two anneals per temperature step so that slope of the resistivity versus time curve, $d\rho/dt$, could be estimated before and after an annealing step from T to $T + \Delta T$. Denoting these slope values $(d\rho/dt)_-$ and $(d\rho/dt)_+$, respectively, E_a can be obtained from the following relation:

$$E_a \approx \frac{k_B T^2}{\Delta T} \log \frac{(d\rho/dt)_-}{(d\rho/dt)_+} \quad (1)$$

where k_B is the Boltzmann constant. It is noted that this method is based on the assumption that a single thermally activated reaction is active at the given temperature and, hence, should be applied with caution.

3. Theoretical methods

Theoretical modelling is based on the following components: (i) DFT calculations are employed for energetic parameters of vacancies, N solutes and their complexes; (ii) α'' nitride precipitation is modelled by classical nucleation and growth theory; (iii) the evolution of N solute, defect and cluster concentrations are described by kinetic rate equations; and (iv) the total resistivity is calculated, taking into account the contribution from nitride precipitates and defects. The methods are briefly described in the next paragraphs.

3.1. Density functional theory calculations

The density functional theory (DFT) calculations were performed with the Projected Augmented Wave (PAW) method [49, 50] as implemented in the VASP (Vienna ab initio simulation package) code [50–52]. $3d$ and $4s$ electrons are considered as valence electrons for Fe atoms, and $2s$ and $2p$ states are considered for N. We employed the Generalized Gradient Approximation (GGA) with the Perdew-Burke-Eruzerhof (PBE) scheme [53]. All the calculations were spin polarized within the collinear approximation. The plane-wave basis cut-off was set to 500 eV. The convergence cut-off for the electronic self-consistency loop was set to $\Delta E = 10^{-6}$ eV. All the results presented below are obtained using a 4×4×4 cubic unit-cell of 128 bcc-Fe sites . We employed a $4 \times 4 \times 4$ k-points grid, following the Monkhorst-Pack scheme [54]. The Methfessel-Paxton broadening scheme [55] with a 0.1 eV width was adopted. For structural optimizations, atomic positions, supercell shape and size were fully relaxed to ensure a maximum residual force of 0.02 eV/Å and a maximum residual stress of 0.1 kbar.

A N interstitial migration barrier was calculated using the Nudged Elastic Band (NEB) method [56, 57]. We set three NEB images between two nearest octahedral interstitial sites, the saddle-point configuration being the N at a tetrahedral site.

We also performed phonon-frequency calculations in order to determine binding free energies between vacancy and nitrogen solutes. The vibrational entropies were obtained within the harmonic approximation from frozen phonon calculations using the VASP and PHONOPY [58] codes. Before the phonon calculations, the 128-sites supercells were fully relaxed with a maximum residual force of 0.001 eV/Å and a maximum residual stress of 0.1 kbar.

3.2. Precipitation kinetics

Precipitation of the metastable α'' nitride is modelled by classical nucleation and growth theory [59] utilizing the formulation given in [60]. The precipitates are regarded as oblate spheroids with half-axes $a > c$ and a constant aspect ratio

$\epsilon = c/a = 0.05$. The driving force for precipitation is the free energy change per unit volume of the α'' phase, Δg, which in the case of dilute alloys can be approximated by

$$\Delta g = \frac{k_B T}{V_{at}} X_N^p \log\left(X_N^m / X_N^{eq}\right) - \epsilon A, \tag{2}$$

where k_B is the Boltzmann constant, T denotes the temperature, V_{at} is the atomic volume (considered here equal in both phases), $X_N^{m,p}$ are the atomic concentrations of N in the matrix and the precipitate, respectively, X_N^{eq} is the equilibrium N matrix concentration and ϵA is elastic self-energy of the coherent α'' particle.

The critical nucleation energy is approximately

$$W^* = \frac{16\pi}{3} \frac{\bar{\gamma}^3}{\epsilon^2 \Delta g^2} = \frac{4\pi}{3} a^{*2} \bar{\gamma}, \tag{3}$$

with $\bar{\gamma} = \frac{1}{2}(\gamma_f + \epsilon\gamma_e)$ the effective interfacial energy, where γ_e and γ_f are the specific interfacial energies of the edge and the flat top of the particle, respectively [61], and a^* is the large half-axis of critical nuclei.

The nucleation rate is calculated by the classical Becker-Döring expression:

$$\frac{dN_p}{dt} = Z\beta^* \exp\left(-\frac{W^*}{k_B T}\right) \tag{4}$$

where N_p denotes the number of nuclei per atomic site, Z is the Zeldovich factor and $\beta^* = 8\pi a^{*2} D_N X_N^m / a_0^4$ is the attachment rate of solutes on a precipitate of critical radius with D_N the diffusion constant of N in α-Fe and a_0 the lattice constant. A detailed expression for Z can be found in [60].

Precipitates grow by incorporating solute atoms from the surrounding matrix. The evolution of the average size, $\bar{a}$, is described by:

$$\frac{d\bar{a}}{dt} = \frac{2D_N}{\pi\epsilon\bar{a}} \frac{X_N^m - X_i}{X_N^p - X_i} - \frac{1}{N_p}\frac{dN_p}{dt}(\bar{a} - a^*). \tag{5}$$

The first term on the right describes the growth of the oblate spheroidal precipitates due to the influx of N atoms from the matrix [60]. X_i is the solute concentration at the matrix/precipitate interface as modified by the Gibbs-Thomson effect [62]:

$$X_i = X_N^{eq} \exp\left(\frac{2\bar{\gamma} V_{at}}{\epsilon\, a\, k_B T X_N^p}\right). \tag{6}$$

The second term on the right of eq. (5) accounts for the reduction of $\bar{a}$ due to the nucleation of new critical nuclei [63].

3.3. Defect reactions

The evolution of point defect and solute atom concentrations is described by a set of reaction rate equations. Recombination and clustering processes are considered as binary reactions of the type:

$$A + B \underset{k^-}{\overset{k^+}{\rightleftarrows}} C, \tag{7}$$

where k^+ and k^- stand for the formation and dissociation rate constants, respectively. The time evolution of each species concentration due to such a reaction is described by:

$$\frac{dX_C}{dt} = -\frac{dX_{A,B}}{dt} = k^+ X_A X_B - k^- X_C. \tag{8}$$

where X_Y denotes the atomic concentration of Y. k^+ is determined by the diffusion of reactants towards each other [64] and is given by:

$$k^+ = 4\pi\, r_{AB}\, (D_A + D_B)\, V_{at}^{-1}, \tag{9}$$

where D_A and D_B are the diffusion coefficients of species A and B, respectively, and r_{AB} is the reaction radius. Detailed balance requires that

$$k^- = k^+ e^{-\Delta G_b / k_B T}, \tag{10}$$

where $\Delta G_b = G_A^f + G_B^f - G_C^f$, with G_Y^f denoting the Gibbs free energy of formation for species Y.

Additionally, there are two balance equations that have to be considered. The first one concerns the total amount of N atoms in the system, X_N^0, which is distributed among the matrix, the α'' precipitates and the V-N clusters:

$$X_N^0 = F_p\, X_N^p + (1 - F_p)\left[X_N^m + \sum_{n,k\geq 1} k\, X_{V_n N_k}\right] \tag{11}$$

where $F_p = \frac{4}{3}\pi a^3 \epsilon N_p$ is the precipitate volume fraction and $X_{V_n N_k}$ denotes the concentration of vacancy-N clusters. SIA-nitrogen complexes are not considered in our model. The second equation derives from the fact that we consider removal of point defects only via SIA-vacancy recombination. Other defect sinks such as grain boundaries and dislocations are expected to have a much lower strength due to the well-annealed state of our samples and are neglected. Thus, the total number of SIAs equals that of vacancies, regardless if they are single or clustered. We can express this as

$$\sum_{n\geq 1} n\, X_{I_n} = \sum_{n'\geq 1} n'\, X_{V_{n'}} + \sum_{n'',k\geq 1} n''\, X_{V_{n''}N_k} = X_{FP} \tag{12}$$

where X_{FP} denotes the effective total FP concentration.

The set of rate equations for the defect concentrations together with the balance equations (11), (12) and the precipitate nucleation and growth equations, (4) and (5), respectively, are integrated numerically by standard algorithms available in the OCTAVE computing environment [65]. The relevant simulation code and results can be found in [66].

3.4. Electrical resistivity calculation

In order to make a direct quantitative comparison to the experimental results we calculate the total resistivity taking into account the contribution from irradiation defects and clusters, N solute atoms and α'' precipitates. The resistivity of an alloy during second phase precipitation exhibits generally a complex behaviour since conduction electron scattering depends on the density, shape and size of precipitates as well as on the precipitate/matrix interface structure. In the present case, where only the early stages of precipitation are considered ($F_p \ll 1$),

the resistivity can be approximated by a simple law of mixtures [67]:

$$\rho = \rho_m\,(1 - F_p) + \rho_p\,F_p \approx \rho_m + \rho_p\,F_p, \tag{13}$$

where ρ_m and ρ_p are the resistivity of the alloy matrix and the precipitates, respectively. These are written in terms of defect and N concentrations as:

$$\begin{aligned}\rho_m = \rho_{\mathrm{Fe}} + \rho_N^m\,X_N^m + \sum_{n\geq 1}\rho_{I_n}\,X_{I_n} \\ + \sum_{n'\geq 1}\rho_{V_{n'}}\,X_{V_{n'}} + \sum_{n'',k\geq 1}\rho_{V_{n''}N_k}\,X_{V_{n''}N_k},\end{aligned} \tag{14}$$

$$\rho_p = \rho_N^p\,X_N^p, \tag{15}$$

where ρ_{Fe} denotes the resistivity of the α-Fe matrix, ρ_N^m and ρ_N^p are the resistivity contributions per N atom in solid solution and precipitates, respectively, ρ_{I_n} and $\rho_{V_{n'}}$ represent the resistivities of V and SIA clusters, respectively, and $\rho_{V_nN_k}$ is the resistiviy of vacancy-nitrogen clusters. It has been assumed according to Matthiessen's rule that conduction electron scattering from all these objects is additive. ρ_{Fe} contains the contribution from phonons and residual impurities in the matrix.

Initially there are no irradiation defects and the total N concentration is assumed to be dissolved in the matrix, thus, the resistivity is equal to:

$$\rho_0 = \rho_{\mathrm{Fe}} + \rho_N^m\,X_N^0. \tag{16}$$

In order to calculate the deviation, $\Delta\rho = \rho$ - ρ_0, we make the following approximation, as often done in similar work [15, 28]: the contribution of V and SIA clusters is considered equal to the sum of the resistivity of individual defects, i.e., $\rho_{V_n} = n\rho_V$ and $\rho_{I_n} = n\rho_I$. Furthermore, $\rho_V + \rho_I = \rho_{FP}$, where ρ_{FP} is the FP resistivity. With this approximation and taking also into account the balance relations (11)-(12) we finally obtain:

$$\begin{aligned}\Delta\rho \simeq \rho_{FP}X_{FP} + \sum_{n,k\geq 1}\left(\rho_{V_nN_k} - n\rho_V - k\rho_N^m\right)X_{V_nN_k} \\ - \left(\rho_N^m - \rho_N^p\right)F_p\,X_N^p.\end{aligned} \tag{17}$$

4. Experimental results

4.1. Resistivity recovery in the range 30 K to 350 K

Fig.1 shows the resistivity recovery of pure and N doped Fe during post-irradiation isochronal annealing as function of temperature up to 350 K. For each curve the total resistivity increase after irradiation, $\Delta\rho_0$, is indicated. The corresponding dose values can be found in Table 2. As can be seen in the figure, the three Fe-N specimens exhibit an almost identical recovery as a function of temperature, despite the significant difference in dose. On the other hand, there are marked differences with respect to the recovery of pure Fe. It is observed that above 110 K the recovery in Fe-N slows down and the curves start to deviate from that of Fe. This continues up to about 280 K, whereupon Fe-N exhibits a region of faster recovery which brings it closer to the pure Fe curve. At 350 K Fe exhibits almost full recovery, whereas in Fe-N a small fraction (< 5%) of the initial resistivity is still present.

Table 3: Resistivity recovery stage data in 5 MeV proton irradiated Fe and Fe-N: stage peak temperature, $\hat{T}$, total recovery, A, and measured activation energy, E_a.

Stage	$\hat{T}$ (K)		A (%)		E_a (eV)
	Fe	Fe-N	Fe	Fe-N	Fe-N
I_A	52	54	3.5	2.2	-
I_B	68	69	4.2	5.0	-
I_C	87	89	3.6	6.9	-
I_D	108	107	54.9	41.6	0.38
I_E	126	-	3.6	-	-
II	164	161	7.7	12.5	0.55
III_A	187	-	4.6	-	-
III_B	216	195	7.6	14.2	0.68
N-stage	-	300	-	15.0	0.78

In general, the recovery in both materials is not continuous but shows distinctive temperature regions of high recovery rate, which are called stages. These can be clearly seen in fig. 2 where the recovery rate is presented as a function of annealing temperature for pure and N-doped Fe at the lowest irradiation dose. The recovery stages have been identified on this figure with reference to previous work on pure Fe [10, 28] and are described in the following paragraphs. Table 3 summarizes the relevant experimental data for each stage: temperature of recovery rate maximum, $\hat{T}$; total stage recovery, A, determined approximately by a graphical method; activation energy, E_a, estimated by the slope-change technique.

The temperature range between 40 and 150 K is characterized as stage I recovery and comprises of several sub-stages. The features observed in fig. 2 at 52, 68 and 87 K in Fe are identified as the sub-stages I_A, I_B and I_C reported by Takaki *et al.* [10] at similar temperatures in electron irradiated high-purity Fe. These features appear also in Fe-N approximately at the same temperatures. The sub-stages I_A to I_C have been previously attributed to the spontaneous recombination of close Frenkel pair (FP) configurations.

The peak at 108 K and the feature on its right side at 126 K observed in fig. 2 for Fe are identified as the sub-stages I_D and I_E, which were also reported earlier [10] and have been ascribed to FP recombination through correlated and long range SIA migration, respectively. I_D is the strongest recovery stage in Fe and it is generally accepted that it consists of two overlaping parts, I_{D1} and I_{D2} [10, 28]. In the present measurements these two parts are not resolved, thus I_D will be considered as a single stage. The contribution of I_D and I_E to defect recovery in Fe is 54.9% and 3.6%, respectively. In Fe-N I_D is observed at 107 K while there is no indication for the presence of an I_E substage. The corresponding recovery in I_D is 41.6%, significantly lower than in Fe. The activation energy of I_D was found equal to 0.38 eV. This value is higher but comparable to previous experimental results (0.27-0.31 eV [10], 0.32 eV [68]) and agrees with more recent *ab-initio* theoretical values for the SIA migration energy in Fe (0.34 eV [69]).

The temperature range between 160 and 180 K is characterized as stage II recovery in pure Fe. A single peak is seen in

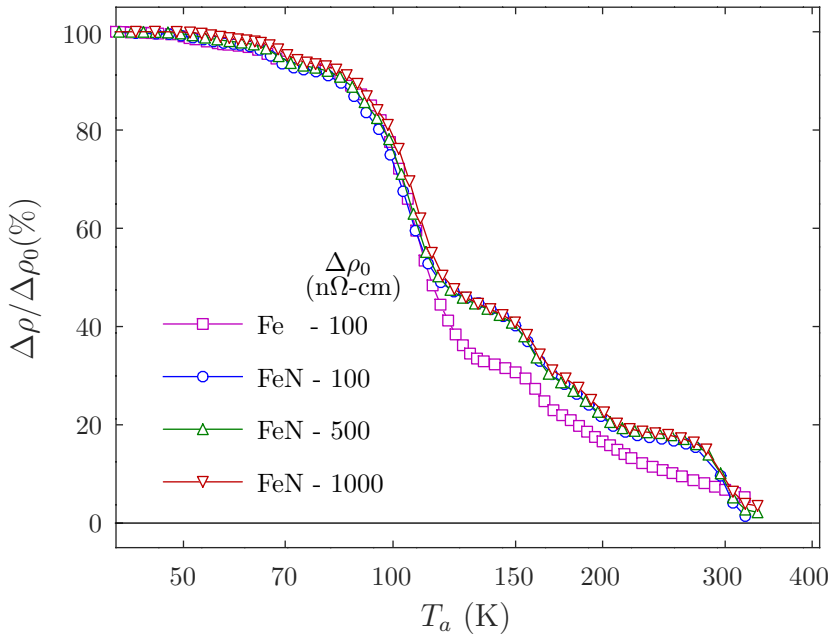

Figure 1: Resistivity recovery of 5 MeV proton irradiated Fe and Fe-N alloys during isochronal post-irradiation annealing as a function of temperature.

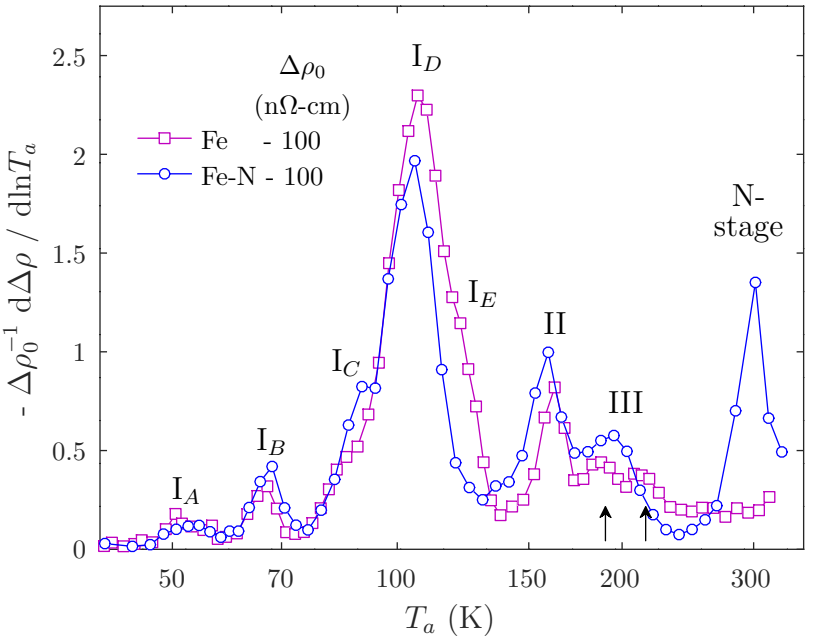

Figure 2: Resistivity recovery rate of pure and N-doped Fe obtained after similar proton irradiation dose level.

fig. 2 at 164 K in the recovery rate of Fe. In Fe-N the peak shifts to lower temperature, 161 K, and exhibits a total recovery of 12.5% which is higher than the corresponding Fe value of 7.7%. The activation energy measured for stage II in Fe-N is equal to 0.55 eV.

The temperature region around 200 K is characterized as stage III. Here Fe exhibits two recovery features at 187 and 216 K, respectively, indicated by the arrows in fig. 2. In Table 3 these are referred to as III_A and III_B, respectively. On the other hand, Fe-N shows a single, wide recovery peak at 195 K. The total recovery corresponding to the Fe-N peak is 14.2% and the activation energy is found equal to 0.68 eV. The combined recovery of III_A and III_B in Fe is 12.2%.

A strong peak is observed at 300 K in the recovery rate of Fe-N whereas Fe exhibits a continuous recovery background in this temperature range. Thus, it is evident that the peak is due to

the presence of N and we will refer to it as the N-stage. As seen from fig. 1, it is associated with a significant resistivity reduction (15%) and its activation energy is 0.78 eV. This value is in good agreement with the N migration barrier in α-Fe as previously obtained experimentally (0.74 eV [70]) and theoretically (0.72 eV [19]). Therefore, this stage is most probably related to the migration of N atoms and their interaction with irradiation induced sinks. The resulting N-containing defect complexes are associated with a reduced specific resistivity contribution.

4.2. Resistivity evolution in Fe-N from 350 K to 550 K

Fig. 3 shows the electrical resistivity variation, $\Delta\rho$, as a function of annealing temperature for one un-irradiated (indicated by $\Delta\rho_0 = 0$) and three irradiated Fe-N alloys at different initial dose. The data are displayed starting from $T = 250$ K so that the N-stage observed at 300 K in the irradiated samples is also included. As seen in the figure, the non-irradiated sample exhibits a characteristic minimum in $\Delta\rho$ in the temperature range between 330 K and 500 K. The resistivity starts to decrease above 330 K and reaches its minimum value $\Delta\rho = -150$ nΩ-cm at $T = 425$ K. Subsequently it increases again and obtains its initial value at about 500 K. Similar results have also been observed previously in resistivity studies of Fe-N alloys in the same concentration range [71, 72]. The behaviour has been attributed to the precipitation of metastable α''-$Fe_{16}N_2$. The nucleation and growth of α'' in the range 330 to 425 K removes N solute atoms from the alloy matrix causing the observed resistivity reduction. Above 425 K the α'' particles become unstable and start to dissolve, releasing the retained N until the initial concentration is established again at 500 K.

In the irradiated Fe-N samples $\Delta\rho$ is initially positive at $T_a = 250$ K due to the presence of radiation defects, which survive after recovery stage III. The value of $\Delta\rho$ at this point is proportional to the initial irradiation dose. As the annealing temperature increases, $\Delta\rho$ exhibits a sharp drop at 300 K, which corresponds to the N-stage observed in figs. 1 and 2. The value of $\Delta\rho$ at the end of the stage, at about 330 K, is again roughly proportional to the irradiation dose.

The effect of irradiation on α'' precipitation is evident from fig. 3 in the temperature range $350 - 550$ K. At the lowest dose level the characteristic resistivity minimum related to α'' nucleation and dissolution is almost unchanged by the presence of radiation defects. However, at intermediate irradiation dose the amplitude of the resistivity minimum is drastically reduced, indicating that radiation defects interfere with α'' precipitation. At the highest dose, the resistivity minimum is totally suppressed and a slight increase of the resistivity is observed in the same temperature range from its value at 330 K. Finally, for all three irradiation doses and at a temperature of about 550 K, the resistivity returns to its pre-irradiation value, i.e., $\Delta\rho \approx 0$. This indicates that there is almost full recovery of irradiation defects and dissolution of precipitates at this temperature. To check this, we subjected the irradiated and 550 K annealed samples to a second isochronal annealing sequence starting at 300 and reaching again 550 K. Fig.4 shows the resistivity evolution in the first and second annealing sequence for the sample irradiated to initial $\Delta\rho_0 = 500$ nΩ-cm. It is observed that the resistivity behaviour during the second annealing is very similar to that of the unirradiated sample. Namely, the broad resistivity minimum between 330 and 480 K is again observed with a large amplitude. This proves that after the 550 K most of the radiation defects and complexes have dissociated and the N solute concentration in the matrix has returned to its initial value. Similar results in the 2nd annealing were obtained for all irradiation dose levels.

5. Simulation results

5.1. DFT calculations of defect parameters

The most relevant parameters of the present model provided by DFT calculations are listed in Table 4. In particular, the dissociation reaction for the VN and the VN_2 clusters:

$$V\mathrm{N} \rightarrow V + \mathrm{N} \tag{18}$$

and

$$V\mathrm{N}_2 \rightarrow V\mathrm{N} + \mathrm{N} \tag{19}$$

are controlled by the Gibbs free binding energy (G_b) corresponding to the reversed reaction plus the migration barrier of the emitted monomer (V or N). The calculated migration barrier is 0.69 eV for a vacancy and 0.72 eV for an isolated N atom. These barriers are in good agreement with previous DFT results [13, 19, 73]. The latter is also consistent with the present experimental data.

The free binding energy, for instance for the $VN + N \rightarrow VN_2$ reaction, is defined as:

$$\begin{aligned}\Delta G_b\left[V\mathrm{N} + \mathrm{N}\right] =& G\left[(p-1)\mathrm{Fe} + \mathrm{N}\right] + G\left[p\mathrm{Fe} + \mathrm{N}\right] \\ &- G\left[(p-1)\mathrm{Fe} + 2\mathrm{N}\right] - G\left[p\mathrm{Fe}\right]\end{aligned} \tag{20}$$

where $G\left[(p-k)\mathrm{Fe} + m\mathrm{N}\right]$, with $k = 0, 1$ and $m = 0, 1, 2$, denotes the Gibbs free energy of a bcc system containing $p - k$ Fe atoms and m N solutes. With the present definition, a positive ΔG_b means an exothermic reaction. The binding enthalpy and the binding entropy are determined using similar expressions.

Consistent with previous DFT studies [74], we find a strong contribution of vibrational entropy to the free binding energy. Therefore, it is important to consider ΔG_b instead of the binding enthalpy for the temperatures considered experimentally. For instance, we obtain a vibrational binding entropy for both $V + \mathrm{N}$ and $V\mathrm{N} + \mathrm{N}$ reactions of respectively 3.55 and 5.61 k_B at 500 K, while the corresponding binding enthalpies are 0.86 and 0.95 eV, respectively. The binding enthalpy for the VN complex is in agreement with previous DFT values [13, 17, 74, 75]. It is noted that discrepancies up to 0.13 eV can occur due to different DFT approximations for, e.g., the pseudopotential or the supercell size. The free binding energies for the resulting VN and VN_2 complexes are presented in Fig. 5 as a function of temperature. As seen from the figure, they are similar for the two clusters in the temperature range of the annealing process. Just above 500 K, they both exhibit a ΔG_b close to 0.7 eV.

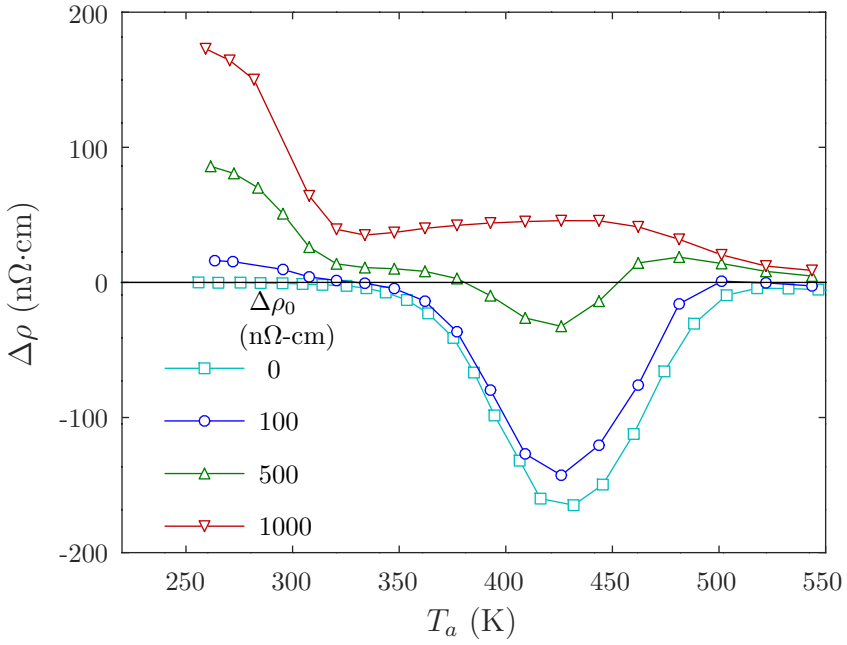

Figure 3: Variation of electrical resistivity as a function of annealing temperature for un-irradiated and proton irradiated Fe-N alloys to 3 different dose levels. $\Delta\rho_0$ is the total irradiation induced resistivity.

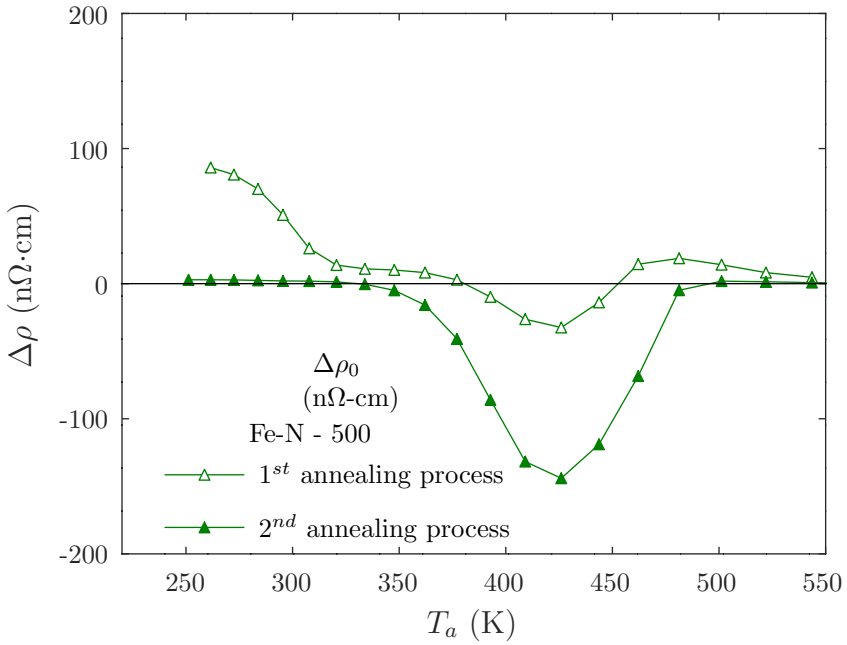

Figure 4: Variation of electrical resistivity as function of the annealing temperature for a proton irradiated Fe-N alloy ($\Delta\rho_0$ = 500 nΩ-cm). After the 1st isochronal annealing up to 550 K the sample was subjected to a 2nd annealing process from 300 K to 550 K.

5.2. Validation of α″ precipitation kinetics modelling

The classical nucleation and growth model of α'' precipitation has been first employed by Sauthoff [60] in his analysis of electron microscopy observations of Fe-N single crystals aged under stress [25]. Although several other groups have reported detailed electrical resistivity studies of early stage α'' nucleation kinetics [71, 72] a similar analysis of their results has not been done. Here we validate and parametrize the precipitation model by comparing to previous isothermal resistivity data of Abiko & Imai [72] and to our isochronal annealing measurements of unirradiated Fe-N.

Key parameters for the modelling are: (a) the diffusion of N

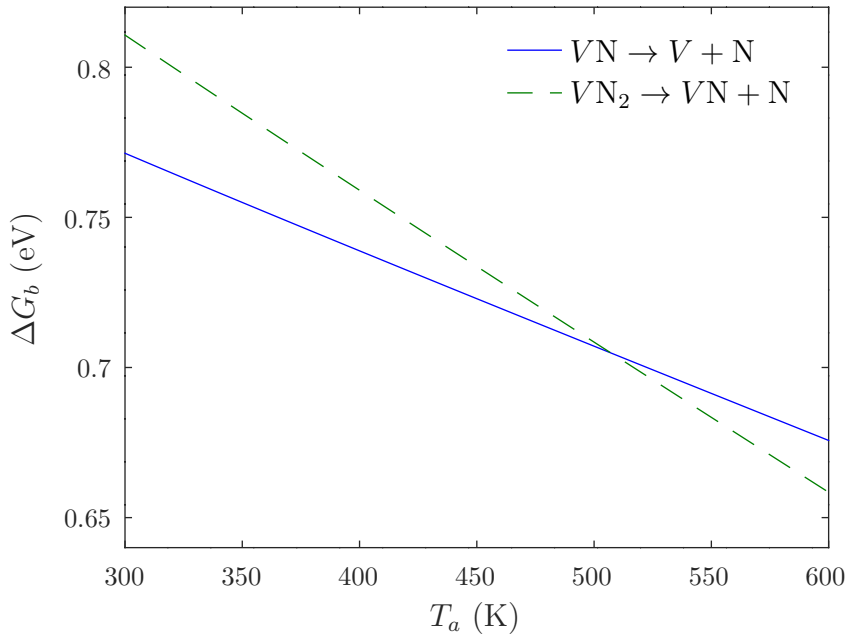

Figure 5: Gibbs free binding energy of VN and VN_2 clusters as a function of temperature as obtained by DFT calculations.

in α-Fe, where the DFT migration barrier of 0.72 eV is used in conjunction with the experimental value $D_N^0 = 0.53$ m^2/s [70] for the pre-exponential factor; (b) the N matrix concentration in equilibrium with the α'' phase, X_N^{eq}, which according to the data evaluation of [76] is described by the empirical relation:

$$X_N^{eq} = X_0^{eq} \exp\left(-\frac{Q_N}{k_B T}\right) \tag{21}$$

with parameters $X_0^{eq} = 2.69$ and $Q_N = 0.365$ eV; (c) the interfacial energy of the α'' particles, $\bar{\gamma}$, which is adjusted in order to fit the experimental data and (d) the resistivity parameters ρ_N^m and ρ_N^p; the value of ρ_N^m is adopted from [34], which gives a value of 7 $\mu\Omega$-cm per at.% N for measurements performed at 77 K and ρ_N^p is adjusted to fit the experiments.

Figure 6 summarizes the simulation results and shows their comparison to experimental data. For the experiment of Abiko & Imai [72], where a supersaturated Fe-N alloy with total N concentration $X_N^0 = 0.088$ at.% was aged at 373 K, the results are depicted in figs 6(a)-(b). Fig. 6(a) shows the simulated time evolution of the fraction of N atoms in solid solution and in the precipitates, X_N^m/X_N^0 and $F_p\, X_N^p/X_N^0$, respectively. The inset displays the corresponding evolution of precipitate volume concentration and size. The calculations correspond to $\bar{\gamma} = 6.9$ mJ/m^2. As seen from the figure, the model predicts the nucleation of α'' precipitates with a final concentration of 2.2×10^{19} m^{-3} at about $t = 50$ min, which grow and attend a final radius of 120 nm at $t \sim 300$ min. These values are in agreement with the experimental observations [72], where an average particle size between 100 and 200 nm and a density of 10^{20} m^{-3} are reported after 1000 min ageing at 373 K. The model predicts that during this process N solute atoms are removed from the matrix until the equilibrium concentration $X_N^m = X_N^{eq}(373\text{K}) = 3.3 \times 10^{-3}$ at.% is attained. At this point the α'' volume fraction is $F_p \approx (X_N^0 - X_N^{eq})/X_N^p = 7.6 \times 10^{-3}$. In fig. 6(b) the resistivity data of Abiko & Imai are directly compared to the simulation. The resistivity drop is essentially due to the N depletion of the matrix as a result of α'' precipitation. At long ageing times, $t \geq 10^3$ min, the experimental resistivity levels off at a minimum value, $\Delta\rho_{min} = -450$ nΩ-cm. From eq. (17) we obtain that $\rho_N^m - \rho_N^p = -\Delta\rho_{min}/F_p X_N^p \approx 5.4\,\mu\Omega$-cm/at.% or $\rho_N^p \approx 0.24\,\rho_N^m$, taking into account the value of ρ_N^m from [34]. The simulated resistivity evolution is in fair agreement with the experimental result. The rate of resistivity variation is slightly higher in the model. This can be due to the various simplifications inherent in the classical nucleation and growth theory. Fig. 6(b) shows calculations for slightly different values of $\bar{\gamma}$ which demonstrate the sensitivity of the model to the interfacial energy parameter.

Figures 6(c)-(d) show simulation results for the isochronal annealing of Fe - 0.048 at.% N in the temperature range 250 to 550 K and compare to our resistivity measurements on an unirradiated sample. In order to apply the nucleation and growth model to this annealing process, the following approximation was employed: during the nucleation phase, if after a temperature increment the existing particles have an average radius smaller than the new critical radius, a^*, then all these particles are considered unstable, they are immediately "dissolved" and nucleation starts from scratch. This ignores a fraction of particles that might have a radius larger than a^* and thus would be stable also at the higher annealing temperature. However, for the current experimental conditions it was confirmed that the fraction of these particles was always very small and could not have a significant effect on the average particle size. In fig. 6(c) the fraction of N atoms in the matrix and in the precipitates are

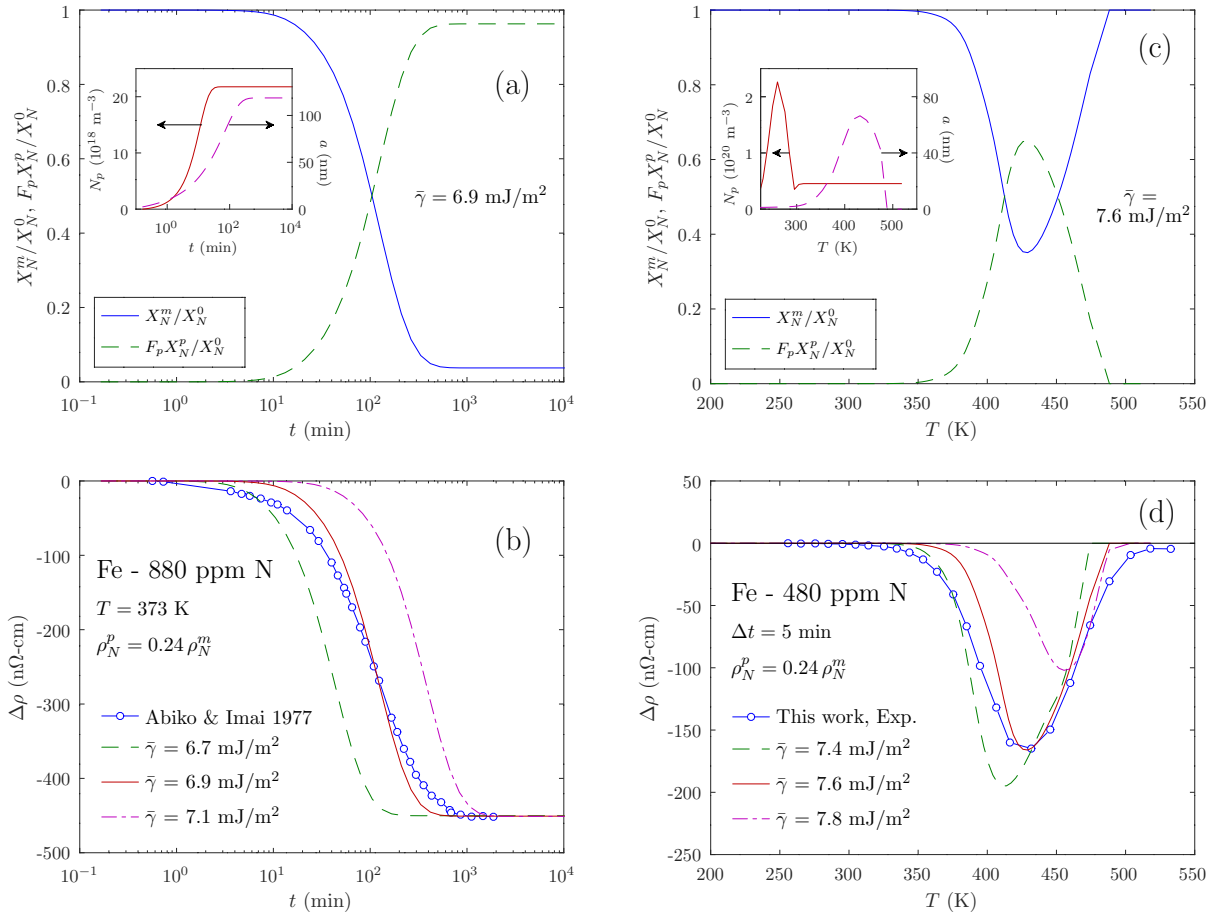

Figure 6: Simulation of nucleation and growth of α'' phase during (a,b) isothermal ageing of a Fe-0.088 at.% N alloy at $T = 373$ K corresponding to the experiment of Abiko & Imai [72] and (c,d) during isochronal annealing of a Fe-0.048 at.% N alloy according to the conditions of the current experiments. (a) and (c) show the evolution of the N fraction in the matrix and precipitates as a function of time and annealing temperature, respectively. The insets in (a) and (c) show the corresponding evolution of particle density and radius. (b) and (d) depict the measured and simulated resistivity evolution as a function of time and annealing temperature, respectively. Symbols correspond to the experimental data and solid curves are model calculations with different values of γ.

shown as a function of annealing temperature. The inset shows the evolution of precipitate density and radius. Significant α'' precipitation starts at about 350 K and precipitates grow up to 430 K. At this temperature about 65% of the N atoms are in the precipitates, which have an average radius $\bar{R} = 66$ nm and concentration $N_p = 4.5 \times 10^{19}$ m^{-}3. Above 430 K the precipitates become unstable and start to dissolve, since the equilibrium N concentration in the matrix is higher and the alloy is no longer supersaturated. At about 500 K all precipitates have dissolved. Fig. 6(b) shows the experimental and simulated resistivity as a function of temperature. Initially the resistivity is reduced due to the depletion of N from the matrix during the α'' nucleation and growth phase. At 430 K the resistivity attains its minimum value and then rises again towards its initial value indicating that all precipitates have been dissolved. The values $\bar{\gamma} = 7.6$ mJ/m^2 and $\rho_N^p = 0.24\rho_N^m$ have been found to best reproduce the position and amplitude of the resistivity minimum. The slightly higher interfacial energy obtained here compared to the isothermal case may be due to a small temperature dependence of $\bar{\gamma}$. As seen in fig. 6(b), the value of $\bar{\gamma}$ is adopted in order to match the resistivity minimum at 430 K and, thus, corresponds to $\bar{\gamma}$ at this temperature. This value will be used in the subsequent simulations of irradiated alloys, since it best describes the isochronal experimental data.

Finally, it is noted that Sauthoff estimated originally a value of $\bar{\gamma} = 9$ mJ/m^2 [60]. The small discrepancy with the values obtained here may be due to the indirect nature of his analysis, which considered only the final precipitate size and density after an elaborate 2-step ageing. In contrast, electrical resistivity measurements used here give information throughout the annealing process.

5.3. Simulation of precipitation in the irradiated Fe-N alloy

The simulation starts at $T \sim 250$ K, i.e., just after recovery stage III. As discussed in detail below, it is assumed that during this stage most mobile vacancies are trapped by N via the reaction

$$V + \mathrm{N} \rightarrow V\mathrm{N}. \qquad (22)$$

leading to a VN cluster concentration X_{VN}^{III}. Due to defect number balance, eq. (12), we have

$$X_{V\mathrm{N}}^{III} = \sum_{n\geq 4} n\, X_{I_n}^{III} = X_{FP}^{III}, \tag{23}$$

where $X_{I_n}^{III}$ are the concentrations of SIA clusters and X_{FP}^{III} denotes the effective number of FPs after stage III.

As the annealing temperature approaches 300 K, N solutes start to migrate and react with VN to form higher order clusters. However, as was shown by the DFT results of Barouh *et al.* [17], $V\mathrm{N}_k$ clusters with $k > 2$ are energetically unfavourable. The current DFT calculations also support this finding. Thus, in our defect simulation we consider only the formation of $V\mathrm{N}_2$ by the following reaction

$$V\mathrm{N} + \mathrm{N} \rightarrow V\mathrm{N}_2. \tag{24}$$

At even higher temperatures the vacancy-N clusters become unstable and begin to dissociate by emitting N atoms until free mono-vacancies are obtained. The latter migrate swiftly and recombine with the remaining SIA clusters according to the reactions

$$V + I_n \rightarrow I_{n-1}, \tag{25}$$

which finally lead to the annihilation of the majority of radiation defects with only a small debris of larger SIA clusters remaining.

The reactions (22), (24) and (25) define a set of rate equations, of the type of eq. (8), for the evolution of defect concentrations. These, together with the nucleation and growth expressions, eqs. (4) and (5), respectively, are employed for the simulation of our experimental results. The parametrization of the rate equations relies mainly on DFT results obtained in the present work and also in [28]. These include the migration energies of vacancies, N solutes and SIA clusters and the temperature dependent dissociation free energies of VN and $V\mathrm{N}_2$. The reaction distances r_{AB}, used in the definitions of forward reaction rates, are taken from previous simulation work: for the reactions between vacancies and SIAs the r_{AB} are taken from [28]; for reactions (22) and (24) we consider the r_{AB} values given in [15] for similar processes involving C instead of N. The vacancy-SIA cluster reaction rate corresponding to eq. (25) is $R_{V-I_n} = 4\pi r_{V-I_n} D_V\, \bar{n}\, X_V \sum_n X_{I_n}$, where $\bar{n}$ is the average cluster size and $\sum_n X_{I_n}$ the total SIA cluster concentration [18]. We assume $\bar{n} \approx 4$ in accordance with previous simulations [28]. The most important parameter values are listed in Table 4.

The purpose of the modelling is to make a quantitative comparison to the experimental results and for that we need to calculate the electrical resistivity from eq. (17). Among the parameters entering this equation we have no information, experimental or theoretical, regarding the resistivity contribution of vacancy-N complexes and specifically the quantities

$$\delta\rho_{V_n\mathrm{N}_k} = \rho_{V_n\mathrm{N}_k} - n\,\rho_V - k\,\rho_{\mathrm{N}}^m, \tag{26}$$

which express the difference in resistivity between a $V_n\mathrm{N}_k$ cluster and a situation where all entities of that cluster exist as separate objects in the α-Fe matrix, at large distances to each other. With the clustering reactions considered in the present model, only two such quantities are needed: $\delta\rho_{V\mathrm{N}}$ and $\delta\rho_{V\mathrm{N}_2}$. Their values will be adjusted to fit the experimental results. We can devise two conditions that these quantities must obey in order to be compatible with the experiment. First, at $T \sim 250$ K, the starting point of the simulation, it is clear for fig. 1 and the data of Table 3 that $\Delta\rho/\Delta\rho_0$ in Fe-N is equal to 17.8% independently of dose. Furthermore, according to our above assumptions, the remaining defects at this point are mainly VN and I_n clusters; thus, from eqs. (17) and (23) we can write the following condition:

$$\frac{\Delta\rho_{III}}{\Delta\rho_0} = \left(1 + \frac{\delta\rho_{V\mathrm{N}}}{\rho_{FP}}\right)\frac{X_{FP}^{III}}{X_{FP}^{0}} = 17.8\%, \tag{27}$$

which couples $\delta\rho_{VN}$ and the effective fraction of FPs surviving stage III, X_{FP}^{III}/X_{FP}^{0}, to the experimentally measured resistivity recovery at the end of stage III, $\Delta\rho_{III}/\Delta\rho_0$. We note here that $\Delta\rho_{III}/\Delta\rho_0$ is dose independent according to experiment and, hence, the same must be true for the ratio X_{FP}^{III}/X_{FP}^{0}.

A second condition can be obtained by observing from fig. 3 that at the highest irradiation dose and in the temperature range 350 to 480 K, the dip in the resistivity that is a characteristic signature of α'' precipitation has disappeared and thus we can assume that precipitation has been fully suppressed. The resistivity in this temperature range, which is almost constant, must be due to SIA and $V\mathrm{N}_{k\leq 2}$ clusters. However, due to the high N concentration, almost all VN clusters have attracted a second N atom during the N migration stage and formed $V\mathrm{N}_2$; thus, in the range 350 to 480 K we have basically only $V\mathrm{N}_2$ clusters. With this assumption, from eq. (17) we can write

$$\Delta\rho_h = \rho_{FP} X_{FP} + \delta\rho_{V\mathrm{N}_2}\, X_{V\mathrm{N}_2}, \tag{28}$$

where $\Delta\rho_h$ is the average high dose $\Delta\rho$ in the aforementioned temperature range, equal to approx. 44 nΩ-cm. Additionally, according to the assumptions of our model, up to about 480 K only the reactions (22) and (24) are active which do not cause defect annihilation and thus the effective number of FPs remains unchanged and equal to X_{FP}^{III}. Hence, the last equation can be rewritten as

$$\frac{\Delta\rho_h}{\Delta\rho_0} = \left(1 + \frac{\delta\rho_{V\mathrm{N}_2}}{\rho_{FP}}\right)\frac{X_{FP}^{III}}{X_{FP}^{0}} = 4.4\%. \tag{29}$$

From eqs. (27) and (29) it is apparent that from the three unknown parameters, $\Delta\rho_{V\mathrm{N}}$, $\Delta\rho_{V\mathrm{N}_2}$ and X_{FP}^{III}/X_{FP}^{0}, only one needs to be adjusted in order for the model to better fit the experimental data. We chose to adjust the ratio X_{FP}^{III}/X_{FP}^{0} and it was found that a value of 24% resulted in the best comparison. The most important aspect that critically defines the choice of X_{FP}^{III}/X_{FP}^{0} is to obtain from the model the same gradual reduction of precipitation as seen experimentally. The final values of all parameters are given in Table 4.

Figure 7 shows the simulation results for the partitioning of N atoms among the Fe matrix, the VN & $V\mathrm{N}_2$ clusters and the α'' precipitates as a function of annealing temperature for the three irradiation dose levels. As it is seen in the figure, the N fraction trapped by vacancies at 250 K doubles at about 300 K

Table 4: List of model parameters.

Parameter	Description	Value	Source
	α'' ($Fe_{16}N_2$) precipitates		
ϵ	Aspect ratio of α'' particle half-axes	0.05	[60]
A	Elastic self-energy of the coherent α'' particle	900 MJ/m^3	[60]
$\tilde{\gamma}$	Effective interfacial energy	7.6 mJ/m^2	Fit (Section 5.2)
	Defect and N solute atom parameters		
D_N^0	Pre-exp. factor for the N diffusion coefficient	0.53×10^{-7} m^2/s	[70]
E_N^m	N Migration barrier	0.72 eV	DFT calc.
D_V^0	Pre-exp. factor for the V diffusion coefficient	1.01×10^{-7} m^2/s	DFT calc.
E_V^m	V migration barrier	0.69 eV	DFT calc.
$\Delta G_b(VN)$	Gibbs free binding energy of VN	Fig. 5	DFT calc.
$\Delta G_b(VN_2)$	Gibbs free binding energy of VN_2	Fig. 5	DFT calc.
	Resistivity calculation		
ρ_{FP}	Frenkel pair resistivity in Fe	3.0 nΩ-cm / appm	[77]
ρ_N^m	N resistivity in Fe matrix	0.6 nΩ-cm / appm	[34]
ρ_N^p	N resistivity in Fe precipitate	$0.24{\cdot}\rho_N^m$	Fit (Section 5.2)
$\delta\rho_{VN}$	VN resistivity difference, eq. (26)	-0.78 nΩ-cm / appm	Fit (Section 5.3)
$\delta\rho_{VN_2}$	VN_2 resistivity difference, eq. (26)	-2.5 nΩ-cm / appm	Fit (Section 5.3)
	Experimental condition		
X_{FP}^{III}/X_{FP}^0	defect ratio after stage III (at $T\sim250$ K)	24%	Fit (Section 5.3)

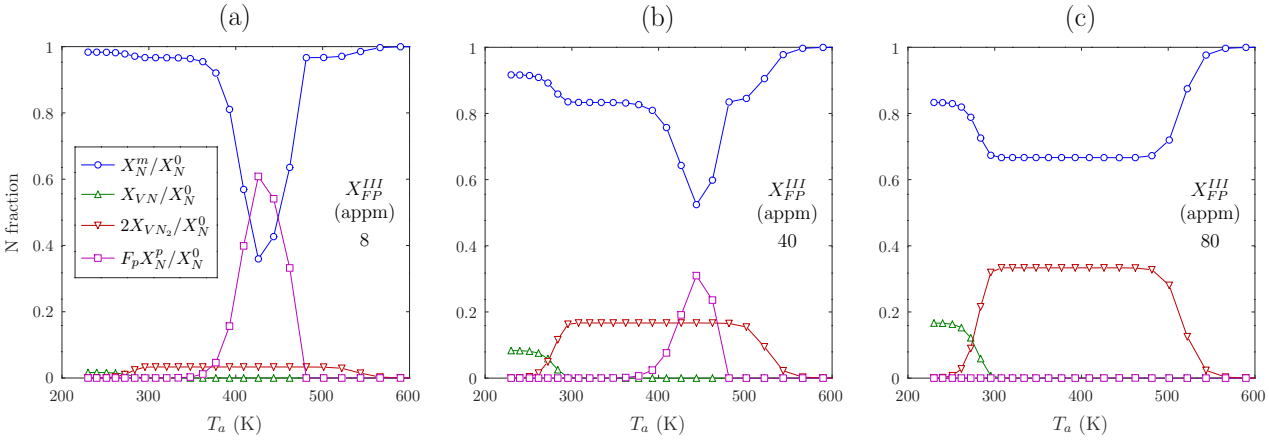

Figure 7: Simulated evolution as a function of temperature of the fraction of N atoms in solid solution, X_N^m/X_N^0, in VN clusters, X_{VN}/X_N^0, in VN_2 clusters, $2X_{VN_2}/X_N^0$, and in α'' precipitates, $F_pX_N^p/X_N^0$, during isochronal annealing of an irradiated Fe-N alloy with initial N concentration $X_N^0 = 0.048$ at.% at (a) low, (b) medium and (c) high dose. The effective atomic concentration of Frenkel pairs at 250 K, after stage III, X_{FP}^{III}, is indicated in each graph.

where VN clusters become VN_2 during the N migration stage. This results in an equal reduction of the N fraction in the matrix. At low dose this reduction only slightly affects the precipitation process. This is evident from a comparison of fig. 7(a) to fig. 6(c) which shows essentially the same quantities in the unirradiated case. When the dose rises to the level corresponding to fig. 7(b), the reduction of free N solutes starts to severely hinder α'' nucleation and finally at the highest dose α'' nucleation is not observed. Above 450 K the precipitates in the low and medium dose start to dissolve and at about 480 K all N from the precipitates is released back to the matrix. At slightly higher temperature, at about 520 K, the VN_2 also dissociate and the N concentration in the matrix goes back to its initial value.

The corresponding simulated evolution of the electrical resistivity is shown in fig. 8 as a function of annealing temperature for the three irradiation doses and the unirradiated alloy. Comparing to the experimental results of fig. 3 it is seen that there is very good agreement and that the model reproduces quantitatively most of the experimental aspects. The simulated $\Delta\rho$ at $T_a = 250$ K are very similar to the experimental ones and scale with dose as expected from eq. (27). The rapid decrease observed between 280 – 300 K corresponds to the N migration stage and the reaction (24). In the experiment this is seen at slightly higher temperatures, 290 – 310 K. After this stage there are essentially only VN_2 clusters and the simulated resistivity levels-off at a value defined by $\delta\rho_{VN_2}$. This corresponds to the measured resistivity at $\sim$ 330 K. In the α'' precipitation region, 350 – 480 K, the characteristic dip of the resistivity is observed in the simulations, as expected, with the minimum occurring at exactly the same temperature, 430 K, and with the same value of $\Delta\rho_{\min}$ as in the experiment. As the irradiation dose increases, the depth of this minimum is reduced. This is also observed experimentally; however, there is a qualitative difference: in the experiment the temperature of the minimum is dose-independent whereas in the simulation it shifts to higher temperatures with increasing dose. At the highest dose precip-

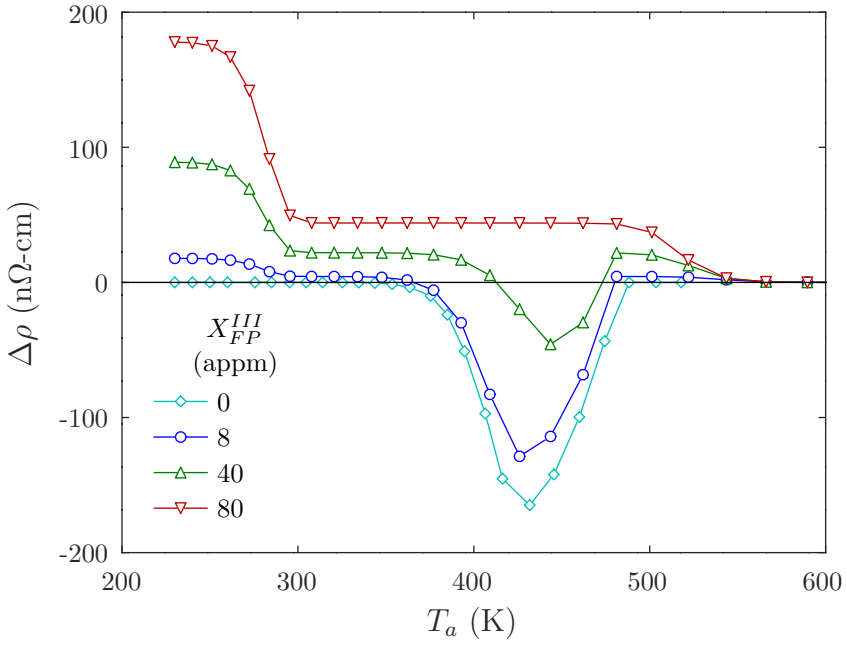

Figure 8: Simulated evolution of the electrical resistivity as a function of temperature of irradiated Fe - 0.048 at.% N during isochronal annealing in the range 250 - 600 K. Results are shown for unirradiated material as well as irradiated to three dose levels leading to the corresponding initial effective Frenkel pair concentration, X_{FP}^{III}.

itation is suppressed and the resistivity dip does not occur. The simulated high-dose resistivity is flat from 310 up to 480 K, whereas, the corresponding experimental curve shows a slight upward variation with temperature in the same region. This behaviour is not captured by the model. Finally, the simulated resistivity curves start to decrease above 500 K and return to $\Delta\rho = 0$ at about 560 K. This is due to the break-up of vacancy-N clusters and the recombination of the released free vacancies with SIA clusters. In the experiment this reduction is seen to start at a slightly lower temperature, $\sim$ 480 K.

6. Discussion

6.1. Resistivity recovery up to 250 K

We discuss here the recovery stages occurring in proton irradiated Fe and Fe-N during isochronal annealing up to 250 K, i.e., up to stage III. An attempt is made to clarify the underlying defect reactions based on comparison to previous experimental and theoretical work. A summary of the most important defect processes for each stage is given in Table 5.

The close-pair stages I_A - I_C are observed at about the same temperature for Fe and Fe-N and these temperatures are in agreement with previous results from electron irradiated pure Fe [10]. However, the total recovery we observe here in these stages, $A_{cp} \approx 11 - 14\%$, is about a factor of 2 smaller than in electron irradiation experiments [10]. This can be understood as follows. Close FP configurations are due to low energy recoils near the displacement threshold. Such events occur frequently in electron irradiation. In contrast, proton irradiation results in much higher recoil energies on the average; thus, the fraction of low energy events and consequently the number of close FPs is significantly reduced.

The largest percentage of defect annihilation in Fe is due to correlated recombination in stage I_D, where SIAs become mobile and after a relatively small number of atomic jumps recombine with their respective vacancies. From the total I_D recovery in Fe, A_D(Fe) = 54.9%, we can obtain an estimate of the average initial SIA-vacancy separation distance, r_p. According to diffusion theory [78] the fraction of FPs undergoing correlated recombination is equal to r_{IV}/r_p, where r_{IV} is the SIA-vacancy recombination radius equal to $3.3\,a_0$ [28]. Excluding close FPs, which recombine before I_D, we can write $r_{IV}/r_p \approx A_D(\text{Fe})/(1 - A_{cp}) = 0.61$ and thus $r_p \approx 5.4\,a_0$. This is higher than the value of $4.3\,a_0$ obtained previously from an analysis of electron irradiation results [79]. The discrepancy can be again attributed to the higher primary knock-on atom (PKA) energy in proton irradiation, which results in a larger initial SIA-vacancy separation.

In Fe-N the total I_D recovery is A_D(Fe-N) = 41.6% while I_E is totally suppressed. The effect of N on I_E has also been observed in electron irradiated Fe-N of similar N concentration [12] and it was attributed to trapping of mobile SIAs at N solutes. Furthermore, in electron irradiated Fe-C [10] the suppression of I_E was reported and attributed to C trapping of SIAs. Jourdan *et al.* [15] simulated these Fe-C resistivity recovery experiments using DFT and kinetic Monte-Carlo methods and showed that C reduces the possibility of $I - V$ recombination due to the formation of $I -$ C complexes. It is expected that N has a similar behaviour. In the present experiments we do not only see the effect of trapping on I_E but we also observe a strong

Table 5: Recovery stages and associated defect reactions in proton irradiated Fe and Fe-N. The fractional recovery is given for reactions that involve defect annihilation. The defect fraction remaining at the completion of each stage is also shown. Numbers in parentheses are based on assumptions discussed in the text.

Stage	T (K)	Defect Reaction	Recovery (%)	Remaining Defects (%)	T (K)	Defect Reaction	Recovery (%)	Remaining Defects (%)
	Fe				Fe-N			
Close FP I_A - I_C	40 - 90	$I + V \rightarrow \varnothing$	11.3	88.7	40 - 90	$I + V \rightarrow \varnothing$	13.8	86.2
I_D	108	$I + V \rightarrow \varnothing$ (Corr.†)	54	33.8	107	$I + V \rightarrow \varnothing$ (Corr.†) $I + \mathrm{N} \rightarrow I\mathrm{N}$ (Corr.†)	41.6	44.6
I_E	120-140	$I + V \rightarrow \varnothing$ (Uncorr.‡) $I + I_{n-1} \rightarrow I_n$ $I + \mathrm{C} \rightarrow I\mathrm{C}$	3.6	30.2	120-140	$I + I_{n-1} \rightarrow I_n$ $I + \mathrm{N} \rightarrow I\mathrm{N}$	-	44.6
II	164	$I\mathrm{C} \rightarrow I + \mathrm{C}$ & $I + V \rightarrow \varnothing$ $I_n + V \rightarrow I_{n-1}$ $I_n + I_m \rightarrow I_{n+m}$	7.7	22.5	161	$I\mathrm{N} \rightarrow I + \mathrm{N}$ & $I + V \rightarrow \varnothing$ $I_n + V \rightarrow I_{n-1}$ $I_n + \mathrm{N} \rightarrow I_n\mathrm{N}$	12.5	32.1
III	187 (A) 221 (B)	$V + V_{n-1} \rightarrow V_n$ (intra-cascade) $V + \mathrm{C} \rightarrow V\mathrm{C}$			195	$I_n\mathrm{N} \rightarrow I_n + \mathrm{N}$ & $I_n + V \rightarrow I_{n-1}$ $V + \mathrm{N} \rightarrow V\mathrm{N}$	(8.1)	(24.0)
N-stage					300	$\mathrm{N} + V\mathrm{N} \rightarrow V\mathrm{N}_2$		(24.0)

† Recombination reaction of spatially correlated defects
‡ Uncorrelated recombination reaction

reduction of I_D. This is attributed to the larger r_p in proton irradiation, which results in increased probability of SIA capture by N atoms during their longer random walk. Correlated recombination in the presence of traps has been studied theoretically by Schroeder [80]. According to his work the reduction of I_D due to trapping, F_D, is

$$F_D \approx 1 - \sqrt{8\pi}\,\frac{r_p - r_{IV}}{a_0}\sqrt{\frac{X_T r_{IT}}{a_0}} \qquad (30)$$

where X_T is the atomic concentration of traps and r_{IT} denotes their capture radius. The last equation is valid for small trap concentrations, where $X_T r_{IT}/a_0 \ll 1$. Setting $F_D = A_D(\text{Fe-N})/A_D(\text{Fe}) \approx 0.76$ according to the present experiments and using the values of r_p and r_{IV} reported in the previous paragraph, it is obtained that $X_T r_{IT}/a_0 \approx 5.2{\times}10^{-4}$ and $r_{IT} \approx 1.1\,a_0$, assuming that X_T is equal to the N concentration in our specimens. This value of r_{IT} is very similar to $1.3\,a_0$ found experimentally for the trapping of SIAs by carbon atoms [10].

The stage II peak observed at 164 K in the recovery of Fe (cf. fig. 2) is very similar to the one observed previously in electron irradiated, carbon-doped Fe [10] with comparable $\Delta\rho_0$, which was attributed to SIA de-trapping from C atoms. Our Fe samples also contain a small concentration of residual carbon impurities (cf. Table 1); thus, the stage II peak can be attributed to the same mechanism. In Fe-N there is significant more trapping of SIA defects due to N, as the above discussion of stage I has shown. It is expected that de-trapping of these defects will also occur in stage II similarly to the de-trapping from C. Indeed, Fe-N exhibits higher recovery in stage II compared to Fe and this can be attributed to de-trapping from N. This has also been assumed by other authors [12]. However, not all of the N-trapped SIAs are released in stage II. If we compare the percentage of retained defects at the end of stage II in Fe-N (32.1%) and Fe (22.5%) we see that Fe-N has about 9.6% more retained defects. These can only be SIAs that remain trapped by N, presumably in higher-order, stable SIA-N configurations, e.g., I_nN with $n = 2, 3$, which form either by capture of mobile small SIA clusters or by re-trapping of single SIAs. A similar assumption has been employed for SIA-C interactions by Jourdan *et al.* in their analysis of resistivity recovery in Fe-C [15]. Based on DFT calculations, these authors obtained a binding energy of 0.2 and 0.33 eV for IC and I_2C, respectively, making the I_2C cluster more stable. If the stage II activation energy of 0.55 eV measured in Fe-N is ascribed to the dissociation of IN complexes, then the resulting binding energy is $E_b(I\mathrm{N}) = 0.21$ eV, taking into account the SIA migration barrier of 0.34 eV [69]. This value of $E_b(I\mathrm{N})$ agrees very well with that reported by Jourdan *et al.* for IC.

The double peak observed in the stage III recovery of Fe is in agreement with previous experiments. Murakami *et al.* [31] observed two peaks at 202 K and 232 K in the recovery of proton ($E = 1$ MeV) irradiated Fe. Matsui *et al.* [81] performed fusion ($E = 14$ MeV) and fission ($E > 1$ MeV) neutron irradiations of ultra pure Fe and found a broad peak between 170 K and 210 K (named II_B) and a second feature between 220 K and 240 K, which they called II_C. In these works the lower temperature peak was attributed either to di-vacancy migration [81] or to intra-cascade vacancy clustering [31]. This is also sup-

ported by the positron annihilation experiments of Hautojärvi *et al.* [82], who observed that the size of vacancy-type defects increases below 200 K in neutron-irradiated pure iron. Thus, we also attribute the III_A stage to intra-cascade vacancy clustering reactions. On the other hand, III_B is most probably associated with long range vacancy migration and subsequent annihilation at immobile SIA clusters or interaction with residual C impurities and formation of stable VC pairs [9, 10, 14, 15].

In stage III recovery of Fe-N only a single feature at 199 K is observed (cf. fig. 2). We assume that it is primarily related to the interaction of mobile vacancies with N resulting in the formation of VN clusters in a manner similar to the vacancy-C reaction [9, 10]. This interpretation has also been proposed in [12] for a stage at 220 K found in electron irradiated, N-doped Fe. The higher N concentration in our specimens accounts for the fact that we observe this feature at a lower temperature. The measured stage III activation energy of 0.68 eV is in agreement with the vacancy migration barrier, $E_V^m = 0.69$ eV obtained in the present DFT calculations and agrees also with previous theoretical predictions [28, 83]. However, it is noted that a lower value for the activation energy, 0.55 eV, has been found earlier in stage III recovery of electron irradiated, ultra pure Fe [10]. Recently, it was suggested that the value of 0.55 eV may correspond to an average of the migration energies of V, V_2, V_3 and V_4 [84]. In addition to vacancy migration, it is possible that in the same temperature range we have also the dissociation of $I_{n\geq 2}$N complexes with subsequent recombination of the emitted SIAs at vacancies. In that case, the observed activation energy of 0.68 eV would correspond to an $I_{n\geq 2}$N binding energy of 0.34 eV, if the SIA migration barrier (0.34 eV [69]) is taken into account. Such a process has been also proposed for $I_{n\geq 2}$C clusters in the Fe-C recovery simulations of [15], where a similar binding energy of 0.33 eV was obtained for I_2C clusters. $I_{n\geq 2}$N dissociation in stage III is also consistent with our model for the subsequent Fe-N resistivity evolution (cf. section 5.3).

6.2. The N recovery stage

The large recovery stage observed at 300 K in Fe-N is most certainly related to the migration of N to irradiation induced sinks. Similar observations have been previously made by a number of workers. Wuttig *et al.* [5] studied neutron irradiated, N doped Fe by means of magnetic disaccommodation techniques and observed the trapping of N at 313 K. Weller and Diehl [7] performed internal friction measurements after neutron irradiation of dilute Fe-N and observed the disappearance of the Snoek peak at 298 K. Finally, magnetic after effect (MAE) spectra of electron and neutron irradiated Fe-120 appm N alloys showed features at 295 K and 310 K, which were also attributed to trapping of N atoms [11]. In these works, the trapping centres where considered to be either vacancies [7, 11] or SIA clusters [5]. On the other hand, Nikolaev & Kurennykh [12] did not detect any similar feature close to 300 K in their resistivity recovery study of electron irradiated, N-doped Fe. These authors observed a peak at 250 K, which they attributed to the dissociation of VN clusters. In the present experiments we do not find evidence for such a recovery feature.

The N stage is very similar to the resistivity recovery stage observed at about 340 K in electron irradiated dilute Fe-C [10]. The slightly higher temperature is due to the lower mobility of C. As has been rightly postulated in earlier works [9] and later confirmed by theoretical modelling [15] the underlying mechanism causing the C recovery stage is the reaction between VC and C towards the formation of VC_2. The present experiments and theoretical modelling show that the behaviour of N is very similar. A direct comparison between experiment and simulation can be done by observing figs. 3 and 8, respectively, in the range 250 to 330 K. The experimentally estimated activation energy of 0.78 eV is only slightly higher that the DFT result (0.72 eV). This is why the simulated stage appears at lower temperature (285 K) than in the experiment (300 K). In comparison, previous experiments indicated a value of 0.74 eV for the N migration barrier in this temperature range [70], while DFT calculations by other workers gave values of 0.79 [13] and 0.72 eV [85].

The good quantitative agreement with respect to the magnitude of resistivity recovery in the N stage is due to the fitted values of $\delta\rho_{VN}$ and $\delta\rho_{VN_2}$ shown in Table 4. Both parameters are negative, i.e., the cluster resistivity is smaller than that of isolated defects. For VN, this can be understood from its DFT predicted configuration, where N relaxes from its octahedral site towards the vacancy, thereby lowering the overall lattice deformation. Similar arguments have been used previously [10, 15] to account for the resistivity of VC. Experimentally it was estimated that the corresponding parameter for C is $\delta\rho_{VC} = -1.2$ nΩ-cm/at.ppm [10]; this is lower that the value obtained here for VN (-0.78 nΩ-cm/at.ppm). For VC_2, the value $\delta\rho_{VC_2} = -0.95$ nΩ-cm/at.ppm has been used in [15], whereas for VN_2 we find here a significantly lower value (-2.5 nΩ-cm/at.ppm). The discrepancy is most probably due to the different configuration of the clusters. In VN_2, DFT shows that the interstitial solutes are positioned symmetrically on both sides of the vacancy, forming a dumbbell parallel to $\langle 001\rangle$. It is expected that this symmetric configuration lowers the overall lattice deformation thereby reducing the resistivity contribution. In contrast, VC_2 does not exhibit this symmetry [17] and consequently the resistivity reduction is not so strong.

6.3. α'' precipitation in irradiated Fe-N

Our experiments show that the presence of a sufficient amount of radiation defects can suppress the nucleation of the metastable α'' phase in a supersaturated Fe-N alloy. This is in agreement with previous high-voltage electron microscopy (HVEM) experiments [6, 8], where Fe-N specimens with N concentration between 0.05 and 0.12 at.% were electron irradiated in the HVEM and subsequently aged at temperatures 400 - 430 K. Precipitates were not observed in the irradiated parts of the specimens, while on the non-irradiated region there was ample nucleation of α'' particles. The authors attributed their findings to trapping of mobile N by vacancies, assuming that vacancies were immobile at the ageing temperature. The present quantitative interpretation of our experiments by a detailed model confirms that indeed it is the interaction between vacancies and N that cause these phenomena. However, a more

detailed picture of the process becomes clear: mobile N and vacancies interact to form immobile VN clusters, which may subsequently accommodate another N atom and become VN_2. The trapped N atoms do not participate in precipitation reactions and this can lead even to a complete suppression of nitride nucleation if the vacancy concentration is sufficiently high. Furthermore, our results show that small defect clusters, either $VN_{k\leq 2}$ or I_n, do not act as nitride nucleation centres.

6.4. Dissociation of vacancy-N clusters

The dissociation of vacancy-N clusters can be better observed in the high-dose irradiation where α'' precipitation does not occur. Fig. 9(a) shows the experimental and simulated resistivity recovery rate in the annealing temperature range $400 \leq T_a < 600$ K. There is a recovery stage observed experimentally at 490 K, while in the simulated curve it is seen at 510 K. The simulation shows that the recovery is due to the break-up of VN_2 and VN complexes and the annihilation of the released vacancies at SIA clusters. Fig. 9(b) shows the simulated evolution of X_{VN} and X_{VN_2} as a function of temperature. It is observed that X_{VN_2} decreases sharply between 480 and 560 K. At the same temperature range, there is a small increase in the concentration of VN, which are intermediate products in the reaction chain of VN_2 dissociation.

As shown in Appendix A, the activation energy associated with the dissociation stage is $Q_d = E_V^m + \Delta G_b[V\mathrm{N}] + \Delta G_b[V\mathrm{N}_2]$. From our DFT results for the VN and VN_2 binding energies (both $\sim$ 0.70 eV at $T \sim 500$ K) and the vacancy migration barrier (0.69 eV) we obtain $Q_d^{\mathrm{DFT}} = 2.1$ eV. This corresponds to the 510 K peak observed in the simulated resistivity data of fig. 9(a). The approximate second-order kinetic law given by eq. (A.7), shown by a continuous curve in fig. 9(a), describes adequately the simulated kinetics. Taking into account the temperature difference $\Delta T = 20$ K from the experimental peak and further assuming that $\Delta Q_d/Q_d \approx \Delta T/T$, we find the corresponding experimental value for the dissociation energy, $Q_d^{\mathrm{Exp}} \approx 2.0$ eV. Hence, there is exceptional agreement between theory and experiment taking into account the relevant measurement and calculation uncertainties.

The observed dissociation temperature is in good agreement with previous experiments. The release of N in the matrix was observed between 490 K [7] and 500 K [5, 11] in electron or neutron irradiated Fe-N. However, the corresponding binding or dissociation energies reported in these works showed large discrepancies. This amplifies the importance of detailed modelling and simulation in order to extract reliable physical parameters from kinetics studies.

7. Conclusions

This paper reports on the findings of an integrated experimental and theoretical study of the interactions between radiation defects and N solute atoms in α-Fe. A supersaturated Fe - 0.048 at.% N alloy has been irradiated with 5 MeV protons at a temperature of 25 K and at three different dose levels. Electrical resistivity measurements were subsequently performed *in-situ* during post-irradiation isochronal annealing up to 550 K. A pure Fe specimen was also studied for comparison. The measurements reveal information on the evolution of radiation defects, their interaction with N and their effect on the precipitation of metastable α''-$Fe_{16}N_2$ nitride. Quantitative modelling of the experimental results was achieved for temperatures $T \geq 250$ K utilizing density functional theory (DFT) for key energetic parameters, kinetic rate equations for the defect reactions and classical nucleation and growth theory to account for nitride precipitation.

From the low temperature ($T < 250$ K) resistivity evolution in irradiated Fe-N the following conclusions can be drawn:

- The resistivity recovery at $T \sim 108$ K is consistent with trapping of mobile SIA defects by N with a trapping radius of 1.1 a_0.
- A part of the N-trapped SIAs is released in stage II, at $T \sim 161$ K, with a binding energy of 0.21 eV.
- Stage III recovery at $T \sim 195$ K is attributed to (i) the trapping of mobile vacancies by N and formation of VN clusters; (ii) the release of remaining N-trapped SIAs, possibly from configurations of type $I_{n\geq 2}$N, with an estimated binding energy of 0.34 eV.

At higher temperatures ($T \geq 250$ K) the experimental observations are well described by the following model:

- As the temperature approaches 300 K, N solute atoms become mobile and interact with VN to form VN_2. Clusters of higher N content are unstable and do not occur.
- Above 300 K and up to 420 K we have the nucleation of metastable α'' nitride precipitates, which then dissolve at higher temperature up to 490 K. If the N matrix concentration is reduced below a certain level due to trapping at vacancies, precipitation may not be observed.
- Above 490 K the VN_2 and VN complexes dissociate and the released vacancies annihilate at SIA clusters.

Regarding the DFT obtained defect parameters, the quantitative comparison between theory and experiment shows the following:

- The DFT calculated N migration barrier of 0.72 eV in α-Fe is entirely consistent with the value of 0.78 eV indicated by the present experiment.
- The results support previous DFT findings that vacancies can trap up to two N atoms forming stable VN and VN_2 complexes.
- For the dissociation of vacancy-nitrogen clusters, DFT calculations result in an activation energy $Q_d = 2.1$ eV, which is the sum of the binding energies of VN (0.70 eV) and VN_2 (0.70 eV) complexes plus the vacancy migration energy (0.69 eV). With this Q_d a recovery stage at 510 K is predicted, while experimentally the stage is observed at 490 K corresponding to an activation energy of 2.0 eV. Hence, the theoretical prediction is in excellent agreement

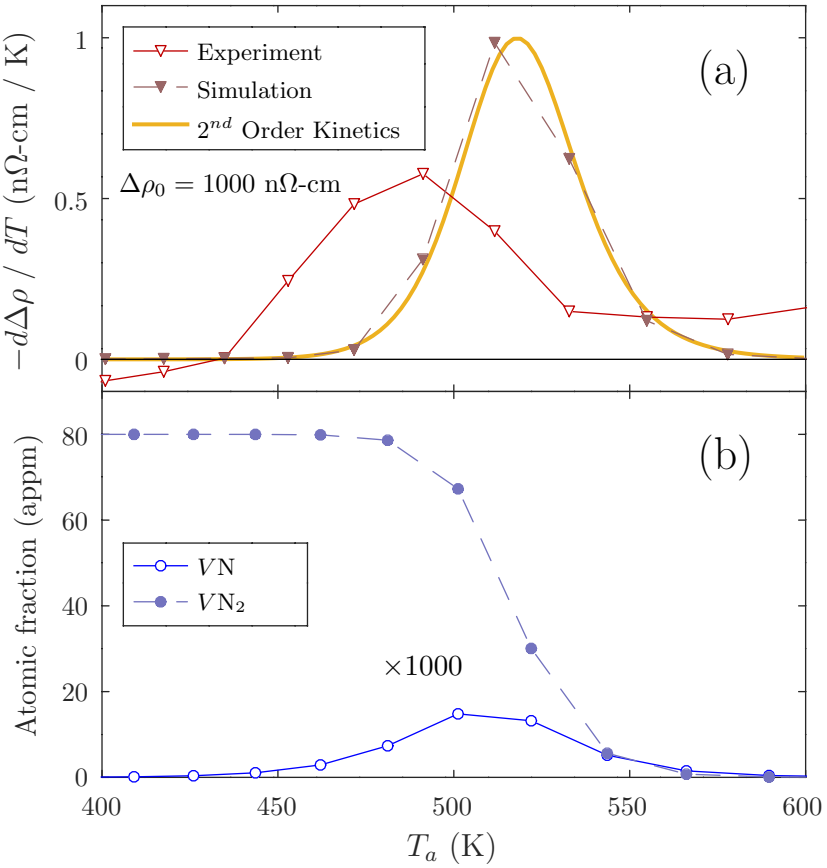

Figure 9: (a) Experimental and simulated resistivity recovery rate of Fe-N irradiated to the highest proton dose for annealing temperature $T_a \geq 400$ K . The recovery stage is due to the dissociation of $VN_{k\leq 2}$ clusters. The continuous curve corresponds to the approximate 2^{nd}-order kinetic law of eq. (A.7). (b) Corresponding simulated evolution of $VN_{k\leq 2}$ cluster concentration.

with the experimental observation. This largely clarifies the previous theoretical-experimental discrepancy regarding the binding energy of vacancy-nitrogen complexes.

Additionally, the following points are also noted:

– The classical theory of nucleation and growth combined with kinetic reaction rate equations can adequately describe precipitation phenomena under irradiation. In the current study, a single phenomenological parameter was employed for this purpose, the precipitate interfacial energy, which was obtained by comparison to experiment.

– The formation of VN and VN_2 clusters is associated with a reduction of the electrical resistivity. Specifically, the values $\delta\rho_{VN} = -0.78$ and $\delta\rho_{VN_2} = -2.5$ nΩ-cm / appm have been obtained for the VN and VN_2 configurations, respectively, where $\delta\rho_{VN_k} = \rho_{VN_k} - \rho_V - k\,\rho_N^m$ with ρ_X the specific resistivity of defect species X in α-Fe.

Acknowledgements

We are indebted to Drs. Chamille Flament and Estelle Meslin, CEA/SRMP, for supplying us with the Fe-N material. We would also like to thank Miltos Adrianis and Vasilis Andreopoulos for assistance during the irradiations.

This work has been carried out within the framework of the EUROfusion Consortium, funded by the European Union via the Euratom Research and Training Programme (Grant Agreement No 101052200 — EUROfusion). Views and opinions expressed are however those of the author(s) only and do not necessarily reflect those of the European Union or the European Commission. Neither the European Union nor the European Commission can be held responsible for them.

We also acknowledge support of this work by the project CALIBRA/EYIE (MIS 5002799), which is implemented under the Action "Reinforcement of the Research and Innovation Infrastructures," funded by the Operational Programme "Competitiveness, Entrepreneurship and Innovation" (NSRF 2014–2020) and co-financed by Greece and the European Union (European Regional Development Fund).

C.-C. Fu thanks for computer resources provided by CINECA-MARCONI supercomputer facility within the SISTEEL project.

Appendix A. $V\mathrm{N}_2$ dissociation rate

The dissociation of $V\mathrm{N}_2$ clusters occurs via the reaction chain shown below together with the respective reaction rates, R_{1-3}:

$$V\mathrm{N}_2 \rightarrow V\mathrm{N} + \mathrm{N}, \quad R_1 = k_1 \left[e^{-\Delta G^b_{V\mathrm{N}_2}/k_B T} X_{V\mathrm{N}_2} - X_{V\mathrm{N}} X_N \right] \quad \text{(A.1)}$$

$$V\mathrm{N} \rightarrow V + \mathrm{N}, \quad R_2 = k_2 \left[e^{-\Delta G^b_{V\mathrm{N}}/k_B T} X_{V\mathrm{N}} - X_V X_N \right] \quad \text{(A.2)}$$

$$V + I_n \rightarrow I_{n-1}, \quad R_3 = k_3 X_V \sum_n X_{I_n} \quad \text{(A.3)}$$

where $k_1 = 4\pi r_{V\mathrm{N}-\mathrm{N}} D_N / V_{at}$, $k_2 = 4\pi r_{V-\mathrm{N}}(D_V + D_N)/V_{at}$ and $k_3 = 4\pi r_{V-I_n} \bar{n}\, D_V / V_{at}$. In such processes, a steady-state is quickly established between the rates of creation and annihilation of intermediate products, here $V\mathrm{N}$ and V; hence, their net rate of change becomes approximately zero:

$$\frac{dX_{V\mathrm{N}}}{dt} = R_1 - R_2 \approx 0, \qquad \frac{dX_V}{dt} = R_2 - R_3 \approx 0. \quad \text{(A.4)}$$

From the last two equations, it is evident that $R_1 = R_2 = R_3$, and we can readily obtain an expression for the $V\mathrm{N}_2$ dissociation rate:

$$\frac{dX_{V\mathrm{N}_2}}{dt} = -R_1 = - \frac{k_1 k_2 k_3 \sum_n X_{I_n} X_{V\mathrm{N}_2} e^{-(\Delta G^b_{V\mathrm{N}} + \Delta G^b_{V\mathrm{N}_2})/k_B T}}{k_2 k_3 \sum X_{I_n} e^{-\Delta G_1/k_B T} + k_1 k_3 X_{\mathrm{N}} \sum X_{I_n} + k_1 k_2 X^2_{\mathrm{N}}} \quad \text{(A.5)}$$

The concentrations of intermediate products are generally much smaller than those of other species, $X_V, X_{V\mathrm{N}} \ll X_{V\mathrm{N}_2}, X_{I_n}, X_{\mathrm{N}}$; thus, from the balance eqs. (11) and (12) we obtain

$$\bar{n} \sum_n X_{I_n} \approx X_{V\mathrm{N}_2}, \qquad X_{\mathrm{N}} \approx X^0_N - 2X_{V\mathrm{N}_2}. \quad \text{(A.6)}$$

Inserting the last two relations in (A.5) and further noting that the first term in the denominator of (A.5) is negligible with respect to the other two, we arrive at the following approximate second-order kinetic law for $V\mathrm{N}_2$ dissociation:

$$\frac{dX_{V\mathrm{N}_2}}{dt} \approx -K_0\, e^{-Q_d/k_B T} X^2_{V\mathrm{N}_2}\, F\left(X_{V\mathrm{N}_2}/X^0_N\right) \quad \text{(A.7)}$$

The dissociation energy Q_d and the rate K_0 are given by

$$Q_d = E^m_V + \Delta G^b_{V\mathrm{N}} + \Delta G^b_{V\mathrm{N}_2}, \quad \text{(A.8)}$$

and

$$K_0 = \frac{r_{V-I_n} D^0_V}{(X^0_N)^2 V_{at}}, \quad \text{(A.9)}$$

respectively, while $F(x) \approx \left(1 - 3x + 2x^2\right)^{-1}$. For the purposes of the present work the approximation $F(x) \approx 1$ was adequate.

References

[1] H. K. D. H. Bhadeshia, R. Honeycombe, Steels: microstructure and properties, Butterworth-Heinemann, 2006.

[2] H. Wagenblast, A. C. Damask, Kinetics of carbon precipitation in irradiated iron, Journal of Physics and Chemistry of Solids 23 (3) (1962) 221–227. doi:10.1016/0001-6160(64)90001-X.

[3] F. E. Fujita, A. C. Damask, Kinetics of carbon precipitation in irradiated iron–II electrical resistivity measurements, Acta Metallurgica 12 (4) (1964) 331–339.
URL http://www.science-direct.com/science/article/B7598-48HRX8V-13T/2/9d2b4c3092ae5a1326a32062f18611f7

[4] H. Wagenblast, F. E. Fujita, A. C. Damask, Kinetics of carbon precipitation in irradiated iron—IV electron microscope observations, Acta Metallurgica 12 (4) (1964) 347–353. doi:10.1016/0001-6160(64)90003-3.

[5] M. Wuttig, J. T. Stanley, H. K. Birnbaum, Interstitial solute trapping in irradiated and quenched iron, Physica Status Solidi (b) 27 (2) (1968) 701–712. doi:10.1002/pssb.19680270227.
URL https://doi.org/10.1002%2Fpssb.19680270227

[6] T. Takeyama, H. Takahashi, The effect of electron irradiation on the precipitation of fe-n alloy, Journal of the Physical Society of Japan 38 (6) (1975) 1783–1783. doi:10.1143/jpsj.38.1783.
URL https://doi.org/10.1143%2Fjpsj.38.1783

[7] M. Weller, J. Diehl, Internal friction studies on reactions of carbon and nitrogen with lattice defects in neutron irradiated iron, Scripta Metallurgica 10 (2) (1976) 101–105. doi:10.1016/0036-9748(76)90129-0.

[8] T. Yamane, J. Takahashi, N. Yamashita, Effect of electron-irradiation on precipitation in fe-n alloy, Radiation Effects 40 (1-2) (1979) 95–96. doi:10.1080/00337577908234499.
URL https://doi.org/10.1080%2F00337577908234499

[9] A. Vehanen, P. Hautojärvi, J. Johansson, J. Yli-Kauppila, P. Moser, Vacancies and carbon impurities in α- iron: Electron irradiation, Phys Rev B 25 (2) (1982) 762–780. doi:10.1103/PhysRevB.25.762.

[10] S. Takaki, J. Fuss, H. Kuglers, U. Dedek, H. Schultz, The resistivity recovery of high purity and carbon doped iron following low temperature electron irradiation, Radiation Effects and Defects in Solids 79 (1983) 87–122. doi:10.1080/00337578308207398.

[11] F. Walz, H. J. Blythe, H. Kronmüller, Binding enthalpies of nitrogen-vacancy complexes in irradiated α-fe, Radiation Effects and Defects in Solids 116 (4) (1991) 339–352. doi:10.1080/10420159108220740.

[12] A. L. Nikolaev, T. E. Kurennykh, On the interaction between radiation-induced defects and foreign interstitial atoms in α-iron, Journal of Nuclear Materials 414 (3) (2011) 374–381. doi:10.1016/j.jnucmat.2011.04.061.
URL http://www.sciencedirect.com/science/article/pii/S0022311511004351

[13] C. Domain, C. S. Becquart, J. Foct, Ab initio study of foreign interstitial atom (c, n) interactions with intrinsic point defects in α-fe, Physical Review B 69 (14) (2004) 144112. doi:10.1103/PhysRevB.69.144112.
URL http://journals.aps.org/prb/abstract/10.1103/PhysRevB.69.144112

[14] K. Tapasa, A. V. Barashev, D. J. Bacon, Y. N. Osetsky, Computer simulation of carbon diffusion and vacancy–carbon interaction in α-iron, Acta Materialia 55 (1) (2007) 1–11. doi:10.1016/j.actamat.2006.05.029.
URL http://www.sciencedirect.com/science/article/pii/S1359645406003703

[15] T. Jourdan, C.-C. Fu, L. Joly, J.-L. Bocquet, M. J. Caturla, F. Willaime, Direct simulation of resistivity recovery experiments in carbon-doped α-iron, Phys Scr 2011 (T145) (2011) 014049. doi:10.1088/0031-8949/2011/T145/014049.
URL http://stacks.iop.org/1402-4896/2011/i=T145/a=014049

[16] D. Terentyev, G. Bonny, A. Bakaev, D. V. Neck, On the thermal stability of vacancy–carbon complexes in alpha iron, J Phys: Condens Matter 24 (38) (2012) 385401. doi:10.1088/0953-8984/24/38/385401.
URL http://stacks.iop.org/0953-8984/24/i=38/a=385401

[17] C. Barouh, T. Schuler, C.-C. Fu, M. Nastar, Interaction between vacancies and interstitial solutes (c, n, and o) in α-fe: From electronic structure to thermodynamics, Phys Rev B 90 (5) (2014) 054112. doi:10.1103/PhysRevB.90.054112.
URL http://link.aps.org/doi/10.1103/PhysRevB.90.054112

[18] D. Terentyev, K. Heinola, A. Bakaev, E. E. Zhurkin, Carbon–vacancy interaction controls lattice damage recovery in iron, Scripta Materialia 86

(2014) 9–12. doi:10.1016/j.scriptamat.2014.04.003.
URL http://www.sciencedirect.com/science/article/pii/S1359646214001481

[19] C. Barouh, T. Schuler, C.-C. Fu, T. Jourdan, Predicting vacancy-mediated diffusion of interstitial solutes in α-Fe, Physical Review B 92 (10) (2015) 104102. doi:10.1103/PhysRevB.92.104102.
URL http://adsabs.harvard.edu/abs/2015PhRvB..92j4102B

[20] M. Gilbert, K. Arakawa, Z. Bergstrom, M. J. Caturla, S. L. Dudarev, F. Gao, A. Goryaeva, S. Hu, X. Hu, R. Kurtz, A. Litnovsky, J. Marian, M.-C. Marinica, E. Martinez, E. Marquis, D. R. Mason, B. Nguyen, P. Olsson, Y. Osetskiy, D. Senor, W. Setyawan, M. Short, T. Suzudo, J. Trelewicz, T. Tsuru, G. S. Was, B. Wirth, L. Yang, Y. Zhang, S. J. Zinkle, Perspectives on multiscale modelling and experiments to accelerate materials development for fusion, Journal of Nuclear Materials 554 (2021) 153113. doi:10.1016/j.jnucmat.2021.153113.
URL https://doi.org/10.1016%2Fj.jnucmat.2021.153113

[21] L. Malerba, M. J. Caturla, E. Gaganidze, C. Kaden, M. Konstantinović, P. Olsson, C. Robertson, D. Rodney, A. Ruiz-Moreno, M. Serrano, J. Aktaa, N. Anento, S. Austin, A. Bakaev, J. Balbuena, F. Bergner, F. Boioli, M. Boleininger, G. Bonny, N. Castin, J. Chapman, P. Chekhonin, M. Clozel, B. Devincre, L. Dupuy, G. Diego, S. Dudarev, C.-C. Fu, R. Gatti, L. Gélébart, B. Gómez-Ferrer, D. Gonçalves, C. Guerrero, P. Gueye, P. Hähner, S. Hannula, Q. Hayat, M. Hernández-Mayoral, J. Jagielski, N. Jennett, F. Jiménez, G. Kapoor, A. Kraych, T. Khvan, L. Kurpaska, A. Kuronen, N. Kvashin, O. Libera, P.-W. Ma, T. Manninen, M.-C. Marinica, S. Merino, E. Meslin, F. Mompiou, F. Mota, H. Namburi, C. J. Ortiz, C. Pareige, M. Prester, R. Rajakrishnan, M. Sauzay, A. Serra, I. Simonovski, F. Soisson, P. Spätig, D. Tanguy, D. Terentyev, M. Trebala, M. Trochet, A. Ulbricht, M.Vallet, K. Vogel, T. Yalcinkaya, J. Zhao, Multiscale modelling for fusion and fission materials: The m4f project, Nuclear Materials and Energy 29 (2021) 101051. doi:10.1016/j.nme.2021.101051.
URL https://doi.org/10.1016%2Fj.nme.2021.101051

[22] K. H. Jack, The occurrence and the crystal structure of α''-iron nitride; a new type of interstitial alloy formed during the tempering of nitrogen-martensite, Proceedings of the Royal Society of London. Series A. Mathematical and Physical Sciences 208 (1093) (1951) 216–224. doi:10.1098/rspa.1951.0155.

[23] K. H. Jack, The synthesis, structure, and characterization of alpha(double prime)-fe16n2, Journal of Applied Physics (ISSN 0021-8979) 76 (1994) 6620–6625. doi:10.1063/1.358482.
URL http://adsabs.harvard.edu/abs/1994JAP....76.6620J

[24] Y. Hong, C. Wu, L. Tian, N. Li, Q. Xu, J. Chen, Microstructure and property evolution of fe-n ferrite undergoing early-stages of precipitation, Materials Science and Engineering: A 696 (2017) 198–207. doi:10.1016/j.msea.2017.04.046.
URL https://doi.org/10.1016%2Fj.msea.2017.04.046

[25] Y. Tanaka, A. Sato, T. Mori, Stress assisted nucleation of α'' precipitates in fe-n single crystals, Acta Metallurgica 26 (4) (1978) 529–540. doi:10.1016/0001-6160(78)90105-0.
URL https://doi.org/10.1016%2F0001-6160%2878%2990105-0

[26] P. Ferguson, K. H. Jack, Stress orientation of nitrogen during the quench-aging of nitrogen ferrite, Philosophical Magazine A 52 (1985) 509–523. doi:10.1080/01418618508237643.
URL http://adsabs.harvard.edu/abs/1985PMagA..52..509F

[27] T. K. Kim, M. Takahashi, New magnetic material having ultrahigh magnetic moment, Applied Physics Letters 20 (12) (1972) 492–494. doi:10.1063/1.1654030.
URL https://doi.org/10.1063%2F1.1654030

[28] C.-C. Fu, J. Torre, F. Willaime, J.-L. Bocquet, A. Barbu, Multiscale modelling of defect kinetics in irradiated iron, Nature Materials 4 (1) (2005) 68–74. doi:10.1038/nmat1286.

[29] B. Gómez-Ferrer, I. García-Cortés, J. F. Marco, D. Jiménez-Rey, R. Vila, Decoupling of defect and short-range order contributions to resistivity recovery measurements in binary alloys, Physical Review B 90 (22) (2014) 220102. doi:10.1103/PhysRevB.90.220102.
URL http://journals.aps.org/prb/abstract/10.1103/PhysRevB.90.220102

[30] G. Apostolopoulos, V. Lukianova, Z. Kotsina, A. Lagoyannis, K. Mergia, S. Harissopoulos, S. Messoloras, The influence of carbon on the resistivity recovery of proton irradiated fe–11 at.% cr alloys, Nuclear Materials and Energy 9 (2016) 465–470. doi:10.1016/j.nme.2016.09.007.
URL https://www.sciencedirect.com/science/article/pii/S2352179115301010

[31] K. Murakami, T. Iwai, H. Abe, N. Sekimura, Y. Katano, T. Iwata, T. Onitsuka, Role of nickel and manganese in recovery of resistivity in iron-based alloys after low-temperature proton irradiation, Philosophical Magazine 95 (15) (2015) 1680–1695. doi:10.1080/14786435.2015.1045568.
URL http://dx.doi.org/10.1080/14786435.2015.1045568

[32] K. Murakami, T. Iwai, H. Abe, N. Sekimura, T. Iwai, H. Abe, N. Sekimura, Y. Katano, T. Iwata, T. Onitsuka, Interaction between solute atoms and radiation defects in fe-ni-si and fe-mn-si alloys under irradiation with proton ions at low-temperature, Journal of Nuclear Materials 482 (2016) 47–52. doi:10.1016/j.jnucmat.2016.10.010.
URL http://adsabs.harvard.edu/abs/2016JNuM..482...47M

[33] D. R. Lide, T. J. Bruno, CRC handbook of chemistry and physics, CRC PressI Llc, 2012.

[34] H. Wagenblast, S. Arajs, Electrical resistivity studies of iron–nitrogen solid solutions, Phys. Status Solidi B 26 (2) (1968) 409–418. doi:10.1002/pssb.19680260203.
URL http://onlinelibrary.wiley.com/doi/10.1002/pssb.19680260203/abstract

[35] S. Harissopulos, M. Andrianis, M. Axiotis, A. Lagoyannis, A. G. Karydas, Z. Kotsina, A. Laoutaris, G. Apostolopoulos, A. Theodorou, T. J. M. Zouros, I. Madesis, E. P. Benis, The tandem accelerator laboratory of NCSR "demokritos": current status and perspectives, The European Physical Journal Plus 136 (6) (6 2021). doi:10.1140/epjp/s13360-021-01596-5.
URL https://doi.org/10.1140%2Fepjp%2Fs13360-021-01596-5

[36] F. Maury, M. Biget, P. Vajda, A. Lucasson, P. Lucasson, Anisotropy of defect creation in electron-irradiated iron crystals, Phys Rev B 14 (12) (1976) 5303–5313. doi:10.1103/PhysRevB.14.5303.
URL http://link.aps.org/doi/10.1103/PhysRevB.14.5303

[37] P. Jung, P. Ehrhart, H. Schultz, H. Ullmaier, Atomic Defects in Metals, Springer-Verlag Berlin Heidelberg, 1991. doi:10.1007/b37800.

[38] P. Ehrhart, Recent advances in huang diffuse scattering, Mat. Res. Soc. 41 (1984) 13–23. doi:10.1557/PROC-41-13.
URL http://journals.cambridge.org/article_S1946427400463293

[39] C. Broeders, A. Y. Konobeyev, Defect production efficiency in metals under neutron irradiation, J. Nucl. Mater. 328 (2–3) (2004) 197–214. doi:10.1016/j.jnucmat.2004.05.002.
URL http://www.sciencedirect.com/science/article/pii/S0022311504004787

[40] J. F. Ziegler, M. D. Ziegler, J. P. Biersack, SRIM – the stopping and range of ions in matter (2010), Nuclear Instruments and Methods in Physics Research Section B: Beam Interactions with Materials and Atoms 268 (11–12) (2010) 1818–1823. doi:10.1016/j.nimb.2010.02.091.
URL http://www.sciencedirect.com/science/article/pii/S0168583X10001862

[41] R. E. Stoller, M. Toloczko, G. S. Was, A. Certain, S. Dwaraknath, F. Garner, On the use of SRIM for computing radiation damage exposure, Nuclear Instruments and Methods in Physics Research Section B: Beam Interactions with Materials and Atoms 310 (2013) 75–80. doi:10.1016/j.nimb.2013.05.008.
URL http://www.sciencedirect.com/science/article/pii/S0168583X13005053

[42] R. E. Stoller, M. Toloczko, G. S. Was, A. Certain, S. Dwaraknath, F. Garner, Erratum to "on the use of SRIM for computing radiation damage exposure" [nucl. instrum. methods phys. res. b 310 (2013) 75–80], Nuclear Instruments and Methods in Physics Research Section B: Beam Interactions with Materials and Atoms 459 (2019) 196–197. doi:10.1016/j.nimb.2019.08.015.

[43] P. Jung, Average atomic-displacement energies of cubic metals, Phys Rev B 23 (2) (1981) 664–670. doi:10.1103/PhysRevB.23.664.
URL http://link.aps.org/doi/10.1103/PhysRevB.23.664

[44] R. E. Stoller, 1.11 primary radiation damage formation, in: Comprehensive Nuclear Materials, Elsevier, Oxford, 2012, pp. 293–332.

[45] M. J. Norgett, M. T. Robinson, I. M. Torrens, A proposed method of calculating displacement dose rates, Nuclear Engineering and Design

33 (1) (1975) 50–54. doi:10.1016/0029-5493(75)90035-7.
URL http://www.sciencedirect.com/science/article/pii/0029549375900357

[46] K. Nordlund, S. J. Zinkle, A. E. Sand, F. Granberg, R. S. Averback, R. E. Stoller, T. Suzudo, L. Malerba, F. Banhart, W. J. Weber, F. Willaime, S. L. Dudarev, D. Simeone, Primary radiation damage: A review of current understanding and models, Journal of Nuclear Materials 512 (2018) 450–479. doi:10.1016/j.jnucmat.2018.10.027.
URL http://adsabs.harvard.edu/abs/2018JNuM..512..450N

[47] C. J. Meechan, J. A. Brinkman, Electrical Resistivity Study of Lattice Defects Introduced in Copper by 1.25-Mev Electron Irradiation at 80 K, Phys Rev 103 (5) (1956) 1193–1202. doi:10.1103/PhysRev.103.1193.
URL http://link.aps.org/doi/10.1103/PhysRev.103.1193

[48] F. Bell, R. Sizmann, Determination of activation energy from step annealing, Physica Status Solidi (b) 15 (1) (1966) 369–376. doi:10.1002/pssb.19660150137.
URL http://onlinelibrary.wiley.com/doi/10.1002/pssb.19660150137/abstract

[49] P. E. Blöchl, Projector augmented-wave method, Phys. Rev. B 50 (24) (1994) 17953–17979. doi:10.1103/PhysRevB.50.17953.
URL https://link.aps.org/doi/10.1103/PhysRevB.50.17953

[50] G. Kresse, J. Hafner, Ab initio molecular dynamics for liquid metals, Phys. Rev. B 47 (1) (1993) 558–561. doi:10.1103/PhysRevB.47.558.
URL https://link.aps.org/doi/10.1103/PhysRevB.47.558

[51] G. Kresse, J. Furthmüller, Efficiency of ab-initio total energy calculations for metals and semiconductors using a plane-wave basis set, Comput. Mater. Sci. 6 (1) (1996) 15–50. doi:10.1016/0927-0256(96)00008-0.
URL http://linkinghub.elsevier.com/retrieve/pii/0927025696000080

[52] G. Kresse, J. Furthmüller, Efficient iterative schemes for ab initio total-energy calculations using a plane-wave basis set, Phys. Rev. B 54 (16) (1996) 11169–11186. doi:10.1103/PhysRevB.54.11169.
URL https://link.aps.org/doi/10.1103/PhysRevB.54.11169

[53] J. P. Perdew, K. Burke, M. Ernzerhof, Generalized Gradient Approximation Made Simple, Phys. Rev. Lett. 77 (18) (1996) 3865–3868. doi:10.1103/PhysRevLett.77.3865.
URL https://link.aps.org/doi/10.1103/PhysRevLett.77.3865

[54] H. J. Monkhorst, J. D. Pack, Special points for Brillouin-zone integrations, Phys. Rev. B 13 (12) (1976) 5188–5192. doi:10.1103/PhysRevB.13.5188.
URL https://link.aps.org/doi/10.1103/PhysRevB.13.5188

[55] M. Methfessel, A. T. Paxton, High-precision sampling for Brillouin-zone integration in metals, Phys. Rev. B 40 (6) (1989) 3616–3621. doi:10.1103/PhysRevB.40.3616.
URL https://link.aps.org/doi/10.1103/PhysRevB.40.3616

[56] H. JÓNSSON, G. MILLS, K. W. JACOBSEN, Nudged elastic band method for finding minimum energy paths of transitions, in: Classical And Quantum Dynamics In Condensed Phase Simulations, World Scientific, 1998, pp. 385–404.

[57] G. Henkelman, B. P. Uberuaga, H. Jónsson, A climbing image nudged elastic band method for finding saddle points and minimum energy paths, The Journal of Chemical Physics 113 (22) (2000) 9901–9904. doi:10.1063/1.1329672.
URL https://doi.org/10.1063/1.1329672

[58] A. Togo, I. Tanaka, First principles phonon calculations in materials science, Scripta Materialia 108 (2015) 1–5. doi:10.1016/j.scriptamat.2015.07.021.
URL https://doi.org/10.1016/j.scriptamat.2015.07.021

[59] R. Wagner, R. Kampmann, P. W. Voorhees, Homogeneous second-phase precipitation, in: G. Kostorz (Ed.), Phase Transformations in Materials, Wiley-VCH, Weinheim, FRG, 2005, pp. 309–407. doi:10.1002/352760264x.ch5.
URL https://doi.org/10.1002/352760264X.ch5

[60] G. Sauthoff, Analysis of the stress orienting of α'' precipitates in Fe-N alloys, Acta Metallurgica 29 (4) (1981) 637–642. doi:10.1016/0001-6160(81)90145-0.
URL https://doi.org/10.1016%2F0001-6160%2881%2990145-0

[61] G. Sauthoff, The influence of external forces on precipitation, Scripta Metallurgica 10 (6) (1976) 557–559. doi:10.1016/0036-9748(76)90261-1.
URL https://doi.org/10.1016%2F0036-9748%2876%2990261-1

[62] M. Perez, Gibbs-thomson effects in phase transformations, Scripta Materialia 52 (8) (2005) 709–712. doi:10.1016/j.scriptamat.2004.12.026.
URL https://doi.org/10.1016%2Fj.scriptamat.2004.12.026

[63] A. Deschamps, F. Livet, Y. Bréchet, Influence of predeformation on ageing in an al–zn–mg alloy—i. microstructure evolution and mechanical properties, Acta Materialia 47 (1) (1998) 281–292. doi:10.1016/s1359-6454(98)00293-6.
URL https://doi.org/10.1016%2Fs1359-6454%2898%2900293-6

[64] T. R. Waite, Theoretical treatment of the kinetics of diffusion-limited reactions, Phys Rev 107 (2) (1957) 463–470. doi:10.1103/PhysRev.107.463.
URL http://link.aps.org/doi/10.1103/PhysRev.107.463

[65] J. W. Eaton, D. Bateman, S. Hauberg, R. Wehbring, GNU Octave version 6.1.0 manual: a high-level interactive language for numerical computations (1 2020).
URL https://www.gnu.org/software/octave/doc/v6.1.0/

[66] A. Theodorou, M. A. Syskaki, Z. Kotsina, M. Axiotis, G. Apostolopoulos, C. C. Fu, (dataset) Interactions of irradiation defects with nitrogen in α-Fe: an integrated experimental and theoretical study (2022). doi:10.5281/zenodo.6418692.

[67] P. L. Rossiter, The electrical resistivity of metals and alloys, Cambridge University Press, Cambridge, 1991.

[68] J. Verdone, W. Chambron, P. Moser, Magnetic anisotropy induced by self-interstitials in low temperature electron irradiated iron, Phys. Status Solidi B 61 (1) (1974) K41–K44. doi:10.1002/pssb.2220610144.
URL http://onlinelibrary.wiley.com/doi/10.1002/pssb.2220610144/abstract

[69] C.-C. Fu, F. Willaime, P. Ordejón, Stability and Mobility of Mono-and Di-Interstitials in α-Fe, Physical Review Letters 92 (17) (2004) 175503. doi:10.1103/PhysRevLett.92.175503.

[70] M. Wasz, R. B. McLellan, Nitrogen diffusion in bcc iron, Scripta Metallurgica et Materialia 28 (12) (1993) 1461–1463. doi:10.1016/0956-716X(93)90575-D.

[71] T. Oi, K. Sato, The reversion phenomenon in iron–nitrogen alloys, Transactions of the Japan Institute of Metals 7 (2) (1966) 129–132. doi:10.2320/matertrans1960.7.129.

[72] K. Abiko, Y. Imai, The precipitation of nitrogen during isothermal aging in a quenched fe–n alloy, Transactions of the Japan Institute of Metals 18 (2) (1977) 113–124. doi:10.2320/matertrans1960.18.113.

[73] A. F. Bialon, T. Hammerschmidt, R. Drautz, Ab initio study of boron in α-iron: Migration barriers and interaction with point defects, Phys. Rev. B 87 (2013) 104109. doi:10.1103/PhysRevB.87.104109.
URL https://link.aps.org/doi/10.1103/PhysRevB.87.104109

[74] M. Posselt, D. Murali, M. Schiwarth, Influence of phonon and electron excitations on the free energy of defect clusters in solids: A first-principles study, Computational Materials Science 127 (2017) 284–294. doi:https://doi.org/10.1016/j.commatsci.2016.10.039.
URL https://www.sciencedirect.com/science/article/pii/S0927025616305572

[75] T. Ohnuma, N. Soneda, M. Iwasawa, First-principles calculations of vacancy–solute element interactions in body-centered cubic iron, Acta Materialia 57 (20) (2009) 5947–5955. doi:10.1016/j.actamat.2009.08.020.
URL https://doi.org/10.1016%2Fj.actamat.2009.08.020

[76] H. A. Wriedt, N. A. Gokcen, R. H. Nafziger, The fe-n (iron-nitrogen) system, Bulletin of Alloy Phase Diagrams 8 (4) (1987) 355–377. doi:10.1007/BF02869273.

[77] O. Dimitrov, C. Dimitrov, A set of mutually consistent values of frenkel-pair resistivities, Radiation Effects 84 (1-2) (1984) 117–129. doi:10.1080/00337578508218437.
URL http://dx.doi.org/10.1080/00337578508218437

[78] H. M. Simpson, A. Sosin, Defect mobility and reaction: Diffusional and rate theory formulations in one and three dimensions, Radiation Effects 3 (1) (1970) 1–21. doi:10.1080/00337577008235611.
URL http://www.tandfonline.com/doi/abs/10.1080/00337577008235611

[79] G. Apostolopoulos, Z. Kotsina, On the analysis of stage i in the resistivity recovery of electron irradiated iron, J. Nucl. Mater. 483 (2017) 142–148. doi:10.1016/j.jnucmat.2016.11.001.
URL http://www.sciencedirect.com/science/article/pii/S0022311516310431

[80] K. Schroeder, Influence of trapping at impurity atoms on diffusion annealing of metals after electron irradiation, Radiation Effects 5 (2) (1970) 255–263. doi:10.1080/00337577008235030.
URL http://www.tandfonline.com/doi/abs/10.1080/00337577008235030

[81] H. Matsui, S. Takehana, M. W. Guinan, Resistivity recovery in high purity iron after fission- and fusion- neutron irradiation, Journal of Nuclear Materials 155 (1988) 1284–1289. doi:10.1016/0022-3115(88)90512-0.
URL http://www.sciencedirect.com/science/article/pii/0022311588905120

[82] P. Hautojärvi, L. Pöllänen, A. Vehanen, J. Yli-Kauppila, Vacancies and carbon impurities in α-iron: Neutron irradiation, Journal of Nuclear Materials 114 (2) (1983) 250 – 259. doi:https://doi.org/10.1016/0022-3115(83)90264-7.
URL http://www.sciencedirect.com/science/article/pii/0022311583902647

[83] C. Domain, C. S. Becquart, *Ab initio* calculations of defects in fe and dilute fe-cu alloys, Phys Rev B 65 (2) (2001) 024103. doi:10.1103/PhysRevB.65.024103.
URL http://link.aps.org/doi/10.1103/PhysRevB.65.024103

[84] Y. Abe, Y. Satoh, N. Hashimoto, Vacancy migration in α-iron investigated using in situ high-voltage electron microscopy, Philosophical Magazine (2022) 1–21doi:10.1080/14786435.2022.2041216.
URL https://doi.org/10.1080%2F14786435.2022.2041216

[85] A. Karimi, M. Auinger, Nitrogen diffusion in vacancy-rich ferrite and austenite, from first principles to applications, Acta Materialia 220 (2021) 117292. doi:10.1016/j.actamat.2021.117292.
URL https://doi.org/10.1016%2Fj.actamat.2021.117292